The Dissertation Committee for Yuxuan Chen Certifies that this is the approved version of the following dissertation:

Transition Metal Dichalcogenide $MoSe_2$ Nanostructures

Committee:

Chih-Kang Shih, Supervisor

Alejandro de Lozanne

Gregory A. Fiete

Qian Niu

Li Shi

Transition Metal Dichalcogenide MoSe2 Nanostructures

by

Yuxuan Chen, B.S.;M.A.

Dissertation

Presented to the Faculty of the Graduate School of

The University of Texas at Austin

in Partial Fulfillment

of the Requirements

for the Degree of

Doctor of Philosophy

The University of Texas at Austin

December 2016

Acknowledgements

I'd like to express my gratitude to a lot of people, who have played important roles in my pursuit of the PhD degree.

First of all, I'd like to thank my parents for supporting me throughout all these years, especially in those stressful and struggling moments. The long distance and the time-zone difference never stopped them from caring for me.

Second, I'd like to thank my supervisor, Dr. Shih, for his patient mentoring and supervising throughout my PhD years. I wouldn't have known the strength and weakness of myself without his help. Besides, he always gave me insightful suggestions both in our weekly meetings and in our nearly daily casual discussions whenever he came down to the lab, which are crucial for the progress of my dissertation projects.

I'd also like to thank the former and current group members of Dr. Shih's lab, who have had overlap with me, for the pleasant collaborating experience and valuable discussions. I'd express my special gratitude to Dr. Chendong Zhang, for the advices and instructions on my projects; and to Qiang Zhang, for his hardworking and the productive collaboration.

My experiments wouldn't have happened without the wonderful work done by the Physics Machine Shop crew, who constructed all my chambers and made a lot of other equipment parts. I also owe a lot of thanks to Jack Clifford and Allan Schroeder, who have taught me machining skills and given me advices in designing and machining.

Last but not the least, I'd like to thank my committee members, Prof. de Lozanne, Prof. Fiete, Prof. Niu, and Prof. Shi, for reviewing my dissertation, and also for the kind advices and reminders in the last a few months.

Transition Metal Dichalcogenide $MoSe_2$ Nanostructures

Yuxuan Chen, Ph.D.

The University of Texas at Austin, 2016

Supervisor: Chih-Kang Shih

Transition metal dichalcogenides (TMDs) are a family of van der Waals (vdW) layered materials exhibiting unique electronic, optical, magnetic, and transport properties. Their technological potentials hinge critically on the ability to achieve controlled fabrication of desirable nanostructures. Here I present three kinds of nanostructures of semiconducting TMD $MoSe_2$, created by molecular beam epitaxy (MBE) and characterized by scanning tunneling microscopy and spectroscopy (STM/STS). The three kinds of nanostructures are two-dimensional (2D) nanoislands, quasi one-dimensional (1D) nanoribbons, and heterostructures. The successful growth of 2D nanoislands lays the foundation for the preparation of the other two structures.

By properly controlling the substrate temperature and Se over-pressure, the $MoSe_2$ atomic layers undergo a dramatic three-stage shape transformation: from fractal to compact 2D nanoislands, and eventually to nanoribbons, in stark contrast to the traditional two-stage growth behaviour involving only the transformation from the fractal to compact regime. Experimentally, it is found that the Se:Mo flux ratio during MBE growth plays a central role in controlling the nanoribbon formation. Theoretically, first-principles calculations show that the abundance/deficiency of extra Se atoms at different island edges significantly modifies the relative step energies between zigzag and armchair edges, which in turn impacts the island shape evolution during nonequilibrium growth.

The successful preparation of MoSe2/hBN/Ru(0001) heterostructure is a demonstration that MBE technique is suitable for fabricating vdW heterostructures. Surprisingly, we found that the quasi-particle gap of the $MoSe_2$ on hBN/Ru is about 0.25 eV smaller than those on graphene or graphite substrates. We attribute this result to the strong interaction between hBN/Ru which causes residual metallic screening from the substrate. The surface of $MoSe_2$ exhibits Moiré pattern that replicates the Moiré pattern of hBN/Ru. In addition, the electronic structure and the work function of $MoSe_2$ are modulated electrostatically with an amplitude of ~ 0.13 eV. Most interestingly, this electrostatic modulation is spatially in phase with the Moiré pattern of hBN on Ru(0001) whose surface also exhibits a work function modulation of the same amplitude.

Table of Contents

List of Tables

List of Figures

Chapter 1: Introduction

The first experimental realization of graphene, a single atomic layer of carbon atoms arranged in a honeycomb lattice, has opened up the field of two-dimensional (2D) materials and 2D electronics[1]. The triumph in graphene has led researchers to create other 2D systems from other layered materials similar to graphite. Transition metal dichalcogenides (TMDs) are a huge family of layered material with diverse electronic properties, including superconductors[2,3], semiconductors, insulators[4], and charge density wave (CDW) states. Transferring the techniques developed on graphene to MoS_2 has led to the discovery of the exotic direct bandgap and huge exciton binding energy in the monolayer (ML) limit[5], while bulk MoS_2 has a much smaller indirect bandgap. In fact, such transition exist in most group-VIB TMDs, namely WS_2, MoS_2, WSe_2, $MoSe_2$. (Without special note, TMD used later in this dissertation only refers to these four compounds.) Moreover, due to strong spin-orbit coupling (SOC) and the similarity with graphene lattice, the theory of valleytronics developed for bilayer (BL) graphene is directly applicable to ML TMDs[6]. The combination of exotic electronic, optical and spin properties in ML TMDs has manifolded the interest in 2D systems. Quite a lot of review articles have sprouted up, covering a wide range of properties, growth[7], optical[8], electronic[9], magnetic[10], and chemical[11], etc. Here in this brief introduction, the relevant results on crystal and electronic structure are discussed.

1.1 Crystal Structure of TMDs

A ball-and-stick model of TMDs is extracted from Ref. 11, and shown in Figure 1.1. Bulk TMDs are layered compounds, with weak van der Waals (vdW) inter-layer coupling and strong intra-layer covalence bonds between transition metal and chalcogen atoms. Each ML has three atomic planes, one plane of hexagonally packed transition metal

sandwiched by two planes of similarly packed chalcogen atoms, resulting in the stoichiometry MX_2 (M: transition metal, X: chalcogen). Each transition metal atom has three M-X bonds on top and three on bottom within the sandwich. Two rotationally inequivalent unit cells can exist, distinguishing the ML lattices into two kinds, 1H (or triangular prismatic, where top and bottom X atoms coincide in the lateral direction) and 1T (or octahedral, where top and bottom X atoms are rotated 180° with any M being the rotational center).

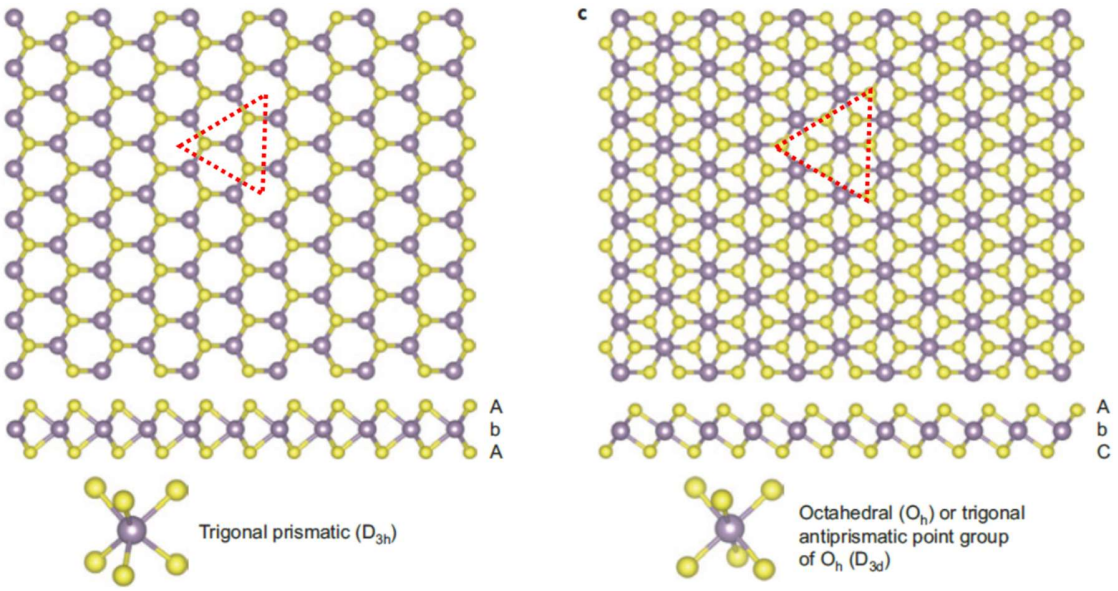

Figure 1.1 Ball-stick model of 1H and 1T structures of ML TMD.

The purple balls are transition metal, while the yellow ones are chalcogen atoms. The figure is reproduced from *Nat. Chem.* **5,** 263–75 (2013).

A few different bulk polytypes exist, too, such as 2H, 3R, 4H, 6R. “In this abbreviated notation, the integer indicates the number of X-M-X sandwiches per unit cell along the hexagonal c axis, while T, H, and R denote trigonal, hexagonal, and

rhombohedral symmetries, respectively"[12]. Figure 1.2 is extracted from Ref. 8 to illustrate 2H and 3R structures, and also the 2D 1st brillouin zone in the reciprocal space. The most stable bulk polytype for group-VIB TMDs is 2H.

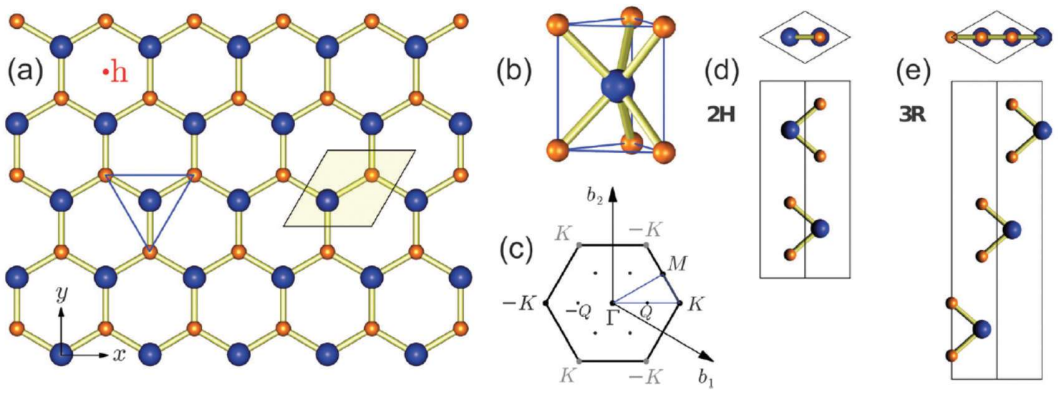

Figure 1.2 Crystal structure and 2D reciprocal lattice of TMDs.

The blue balls represent transition metal atoms, and the orange ones are chalcogen atoms. The rhombus in (a) is the 2D unit cell, and the 2D lattice constant a is equal to the in-plane X-X distance. The figure is reproduced from *Chem. Soc. Rev.* **44,** 2629–2642 (2015).

The lattice constants of group-VIB TMD materials are listed in Table 1.1. Lattice constants a and c are for 2H structure, so the values of c/2 reflect the ML thicknesses. The in-plane lattice constant equals to the distance between nearest neighboring M or X atoms within any of the three atomic planes in a ML. Comparing the a and c values of different TMDs, it can be concluded that, the chalcogen atoms impose a bigger influence on the crystal structure, which makes sense because the transition metal atoms are sandwiched in between two chalcogen planes. However, the bandgap values are influence more by the transition metal species for the ML TMDs, which is discussed below.

	WS_2[13]	MoS_2	WSe_2	$MoSe_2$
Lattice constant a (Å)	3.15	3.16[14]	3.28[14]	3.29[14]
Lattice constant c/2 (Å)	6.15	6.16[14]	6.45[14]	6.48[14]
Quasi-particle bandgap (eV)	2.05	2.15[15]	2.08[16]	2.18[17]
Optical bandgap (eV)	1.95	1.9[5,18]	1.63[19]	1.55[17]

Table 1.1 Lattice constants and band gaps of group-VIB TMD materials.

1.2 Electronic Structure of TMDs

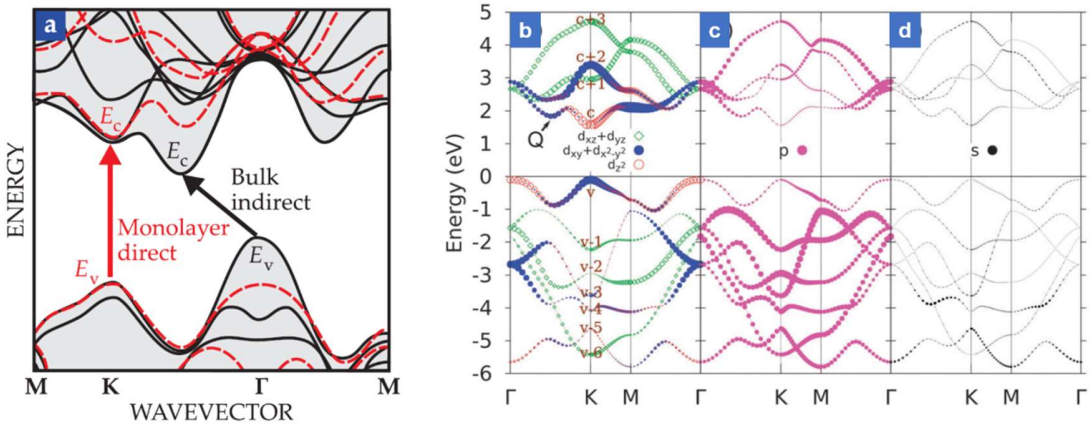

Figure 1.3 Electronic structure of MoS2 from DFT calculation.

Electronic structure of MoS2 from DFT calculation: **a**, ML (red dashed lines) and bulk (black solid lines) bands stacked together. Extracted from *Phys. Today* **69,** 38–44 (2016)[20]. **b-d**, Orbitally resolved band structure, featuring metal *d* orbits, chalcogen *p* orbits and *s* orbits respectively. Extracted from *Chem. Soc. Rev.* **44,** 2643–2663 (2015)[9].

Chemically, the covalence M-X bond are composed of electrons from transition metal *d* orbits and chalcogen *p* orbits, therefore, qualitatively, the lower conduction band edge and the higher valence band edge mainly come from these orbits. However, quantitatively, it is found that the inclusion of metal *s* orbits and the consideration of self-energy correction (GW methods) are the keys for DFT calculation to reflect the ML direct bandgap[9] and a large bandgap values[21,22]. Bulk band structure of TMDs had been studied theoretically and experimentally long before the fever of 2D materials[12,14,23]. Bulk TMDs are indirect bandgap semiconductors, with valence band maximum (VBM) locate at Γ point and conduction band minimum (CBM) located at Q point, which is between K point and Γ point, as shown by the black solid lines in Fig. 1.3a. The contribution of different orbits to the DOS at different high-symmetry points in *k* space are listed in Table 1.2, which is extracted from *Chem. Soc. Rev.* **44,** 2643–2663 (2015). Subscript c and v stands for conduction band and valence band, respectively.

State	Majority of orbits	Minority of orbits
$\mathbf{K_c}$	M-d_{z^2}	X-$p_x,\ p_y$
$\mathbf{K_v}$	M-$d_{x^2-y^2},\ d_{xy}$	X-$p_x,\ p_y$
$\mathbf{Q_c}$	M-$d_{x^2-y^2},\ d_{xy}$	M-d_{z^2}, X-$p_x,\ p_y,\ p_z$
$\mathbf{\Gamma_v}$	M-d_{z^2}	X-p_z

Table 1.2 Majority and minority orbits at different points in k space.

Electronic structure calculations for ML TMDs[21,22,24,25] show that, ML TMDs have direct bandgaps, which originate from the altering of chalcogen p_z orbits at Q point in conduction band and at Γ point in valence band, due to the absence of inter-layer coupling.

To be specific, when the TMD changes from bulk/multilayer to ML, the bond/anti-bond splitting of chalcogen p_z orbits at Q point in conduction band and at Γ point in valence band both reduce significantly, while the metal *d* orbits almost remain intact, probably due to the localized nature of metal *d* orbits inside the sandwich and the delocalized nature of chalcogen p_z orbits exposed on the surface of the sandwich. As a result, VBM changes from Γ point to K point and CBM changes from Q point also to K point, and the bandgap increases, as shown by the red dashed lines in Fig. 1.3a. Photoluminescence (PL) experiments, angle-resolved photoemission spectroscopy (ARPES), and scanning tunneling microscopy/spectroscopy (STM/STS) have all confirmed these statements, shown in Fig. 1.4.

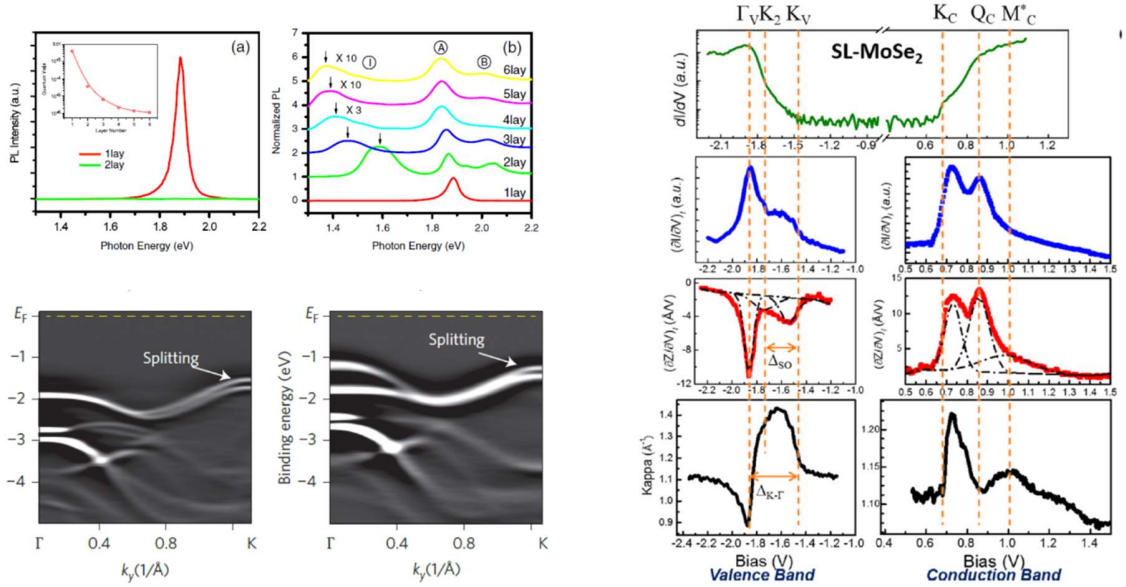

Figure 1.4 Characterization of TMDs.

PL[5] (upper left two panels), ARPES[26] (lower left two panels) and STS[16] (right seven panels) of TMDs.

1.3 SAMPLE PREPARATION

There are mainly three approaches of sample preparation: exfoliation, chemical vapor deposition (CVD), and molecular beam epitaxy (MBE). Exfoliation is most universal, applicable to all vdW layered materials, and the as prepared MLs can be laid upon any substrate. However, this method has difficulty in controlling the size or shape of the ML flakes. CVD has much better control, and it can massively produce large ML films. The drawback is that, **i)** the defect density in CVD samples is much larger than in exfoliated samples, and **ii)** the TMDs can only be grown on a limited number of substrates, and **iii)** the edges of CVD flakes usually trap chalcogen atoms or byproducts of the chemical reaction, and usually there are multilayer nucleation cores at the center of the CVD islands.

MBE is another way of controllably growing TMD MLs. Though it is also selective on substrates, and the flake sizes are usually smaller than those of CVD samples, MBE has a big advantage: it's compatible with *in-situ* UHV characterization, such as STM, which is capable of probing the local electronic properties of the TMD MLs.

1.4 MOTIVATION

Since MBE is a powerful preparation technique, which prevents unintentional doping and contamination, the intrinsic electronic properties of TMDs and their heterostructures can be preserved using MBE method and studied in-situ by STM. Moreover, the expertise we have in MBE, STM, and PL measurements allows us to study TMDs comprehensively and to hopefully provide new insight into the field. Indeed, we are among the first a few groups in the world to prepare $MoSe_2$ MLs using MBE, and we are the first to report the bottom-up fabrication of $MoSe_2$ nanoribbons. The next three chapters present the three aspects of my study of TMD nanostructures.

Chapter 2: Molecular Beam Epitaxy

MBE is a thin film growth technique, which allows *in-situ* growth monitoring and is capable of generating various high-quality single crystal thin films, heterostructures and superlattices with atomically flat surfaces and sharp interfaces. The phrase "molecular beam epitaxy" is self-explaining: "epitaxy" literally means "growing on top"; "molecular beam" indicates the beam nature of the mass flow toward the substrate, which is only possible in high vacuum (HV, 10^{-3} to 10^{-9} Torr) and in ultrahigh vacuum (UHV, $< 10^{-9}$ Torr) environment. Therefore, an MBE system basically consists of UHV environment, sources, and a substrate heating or cooling stage. In order to have precise control of the growth, certain *in-situ* characterization techniques can be implemented, such as reflective high energy electron diffraction (RHEED), Auger electron spectroscopy (AES), ellipsometry, etc.

MBE has been developed and commercialized for decades, and there have been a lot of textbooks on MBE. Therefore, this chapter will only focus on technical details of the home-built Chalcogenide MBE, which was designed and assembled by myself.

Figure 1 shows a schematic illustration of an MBE system, which is also the engineering drawing of the cross-section view of an older version Chalcogenide MBE. As mentioned above, an MBE system usually contains a few sources for reactants (Fig. 2.1a), a sample stage with cooling or heating capability (Fig. 2.1b), and RHEED (Fig. 2.1c-e), and all these are accommodated in a UHV chamber. Since the sources could be in liquid phase during evaporation, the sources are designed to point up, and therefore the sample should be facing down. RHEED electron beam directs to the sample from a low glancing angle, in order to avoid blocking or being contaminated by the sources.

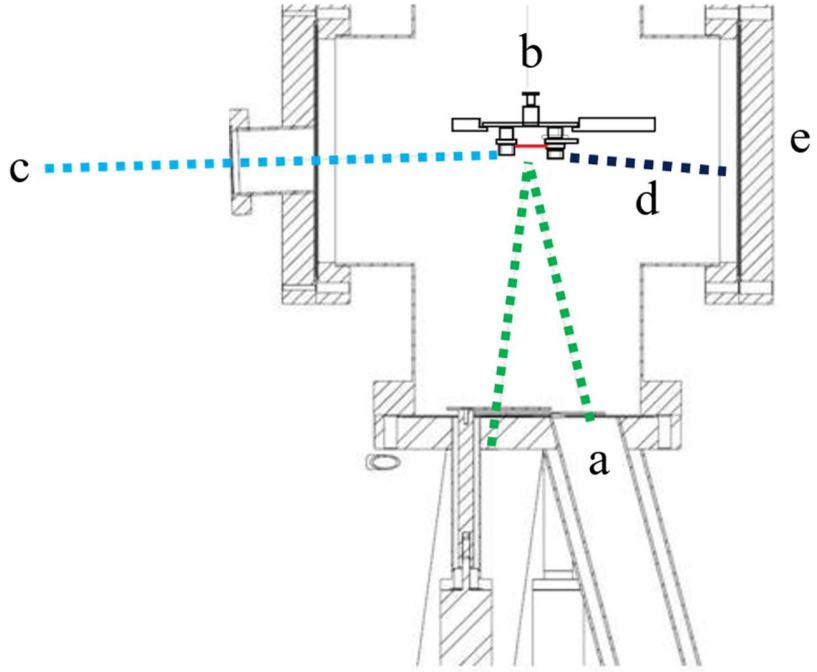

Figure 2.1 Illustration of MBE system.

The contour is an engineering cross-section view of an MBE system. **a**, Sources. The green dashed line indicates the mass flow. **b**, Sample and sample heating /cooling stage (not in scale). **c**, RHEED incident electron beam (cyan dashed line). **d**, RHEED refracted electron beam. **e**, RHEED screen.

2.1 ULTRAHIGH VACUUM

UHV is necessary for MBE, since the beam nature of the mass flow requires a fairly long mean free path of atoms or molecules of reacting substance, while mean free path is reversely proportional to pressure. Using the ideal gas assumption, mean free path can be expressed as:

$$L = \frac{k_B T}{\sqrt{2}\pi d^2} \cdot \frac{1}{p}$$

where k_B is Boltzmann constant, T is temperature of the chamber, d is the diameter of the gas molecule, and p is the pressure. In order to get a mean free path of 1 meter, and by assuming T=300K, and d = 1 Å, one gets $L = 7.5 \times 10^{-4} Torr$, which is in HV range. However, considering the requirement of negligible impurity concentration (1 ppm) and

the low growth rate of most MBE (< 1monolayer / second), the base pressure of a MBE system should be in $10^{-11}Torr$ range.

Though generating UHV has been practiced routinely in our lab, achieving UHV is not a trivial task. The chamber needs to be made by stainless steel (SS), and the connection between different parts of the chamber needs to be in CF (conflat) style. Moreover, the entire SS chamber needs to be cleaned thoroughly and carefully, and then baked to ~ 150 °C for 24-to-48 hours to fully outgas the absorbed gas molecules on the inner surface; otherwise, barely pumping the chamber can at best achieve HV (about $10^{-8}Torr$). At the end of the UHV preparation, the chamber is cooled down to room temperature, and during the cooling, Titanium sublimation pump (TSP) needs to be run repeatedly, to more effectively remove Hydrogen gas, which is the main remnant gas in chamber in HV and UHV. Though the combination of a roughing pump and a large-capacity turbo pump is enough to generate UHV, ion pumps are usually employed as the final-stage pumping, since the ion pumps are mechanically motion free and are ideal for STM and other vibration-sensitive measurements.

2.2 SOURCES OF MOLECULES AND ATOMS

There have been tremendous amount of effort in studying the effusion phenomena and designing appropriate apparatuses for different kinds of source material. Sources in MBE can be primarily categorized into two species: gas sources and solid sources. Gas sources, such as AsH_3, PH_3, and some metal organic compounds, are common for III-V group compounds growth. H_2S gas has been used as early as 1980s in the growth of MoS_2. However, since no gas source is involved in the MBE growth of $MoSe_2$ in my work, only solid sources are discussed here. Solid sources, on the other hand, are much more

frequently used. Two major heating mechanism are utilized for evaporating different solid state materials: the first is usually called effusion cells, which utilize radiation heating by a resistive filament and evaporate source material from a crucible; the second utilizes electron beam (*e*-beam) bombardment either directly on the reactant material themselves, or on special metallic crucibles. In our home-built MBE, there are in total 5 evaporation cells in use, one being *e*-beam heated source for Molybdenum and the other four being effusion cells for Selenium, Tellurium, Bismuth and Iron. Potentially two more sources can be added to this system.

2.2.1 Effusion cells

Basically an effusion cell consists of **i)** a crucible to carry source material, **ii)** wire resisters wrapping around the crucible, **iii)** radiation shielding outside the resisters, and **iv)** a thermal couple attached to the bottom of the crucible for temperature measurement. Figure 2.2 illustrates the structure of a home-built effusion cell. The tungsten filament around the crucible, and the thermal couple attached to the bottom of crucible, are not shown in this illustration. The tungsten filament is made by winding a thin tungsten wire tightly onto the threads of a bolt of the proper size for a suitable amount of rounds, to fit the size of the crucible. In the case of the Se effusion cell, the diameter of the W wire is 0.005”, the bolt is 1/4-28, and the number of rounds is 10.

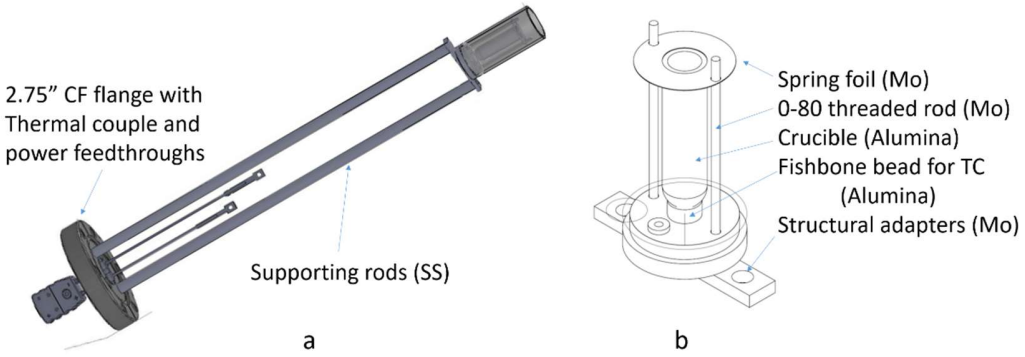

Figure 2.2 Home-built effusion cell.

a, Engineering drawing of a home-built effusion cell assembly. The shields outside the crucible are partial transparent. **b**, Detailed structure of the crucible part.

Various modification can be made to the basic structure to accommodate different material's special properties; for example, Aluminum needs a cold lid, As and S need a "cracker" in front of the orifice of the crucible to break down big molecules and create atoms or smaller molecules.

What makes the MBE effusion cells different from other vacuum deposition sources is their ability to generate films of uniform thickness over an entire substrate of up to a few inches in diameter. This uniformity has a lot to do with the crucible design, and the crucible-to-substrate geometry. The sample stage in commercial MBE systems usually rotates during the growth, to ensure the uniformity. The detailed discussion about crucible design can be found in[27]. In our case, the substrates are much smaller, about 0.4" x 0.1", so the uniformity is not an issue even with the sample stage staying still during the growth,

and the simple home-built effusion cells work just fine. Sometimes people also call effusion cells as *Knudsen cells*, however, they are two different concepts. As long as the opening of a crucible is smaller than the mean free path of the gas beam, which is usually in 1 meter range in MBE, a evaporator can be called an effusion cell. A Knudsen cell, on the other hand, has a special crucible with very small orifice, which is usually less than one tenth of the diameter of the crucible. As a result, the vapor of the source material reaches its equilibrium pressure inside the crucible and at the orifice as well. Such design is suitable for material with low vapor pressure. An effusion cell can be converted to a Knudsen cell simply by adding a lid with a small orifice at the top of the crucible. In my experiments, Se was evaporated from a home-built effusion cell.

2.2.2 E-beam evaporator

For certain material with high evaporation temperature, usually called refractory metals, it is difficult to find a suitable crucible for them, and the radiation heating of the effusion cell could heat up the surrounding stainless steel chamber so much that the chamber starts to outgas significantly, which can cause impurity in the sample. Unfortunately, Mo and W both fall into this category, introducing a challenge to the MBE growth. In these cases, one would prefer a heating mechanism which can focus the heat only on the evaporation surface, and avoid causing the environment outgassing. Electron-beam heated sources satisfy this demand.

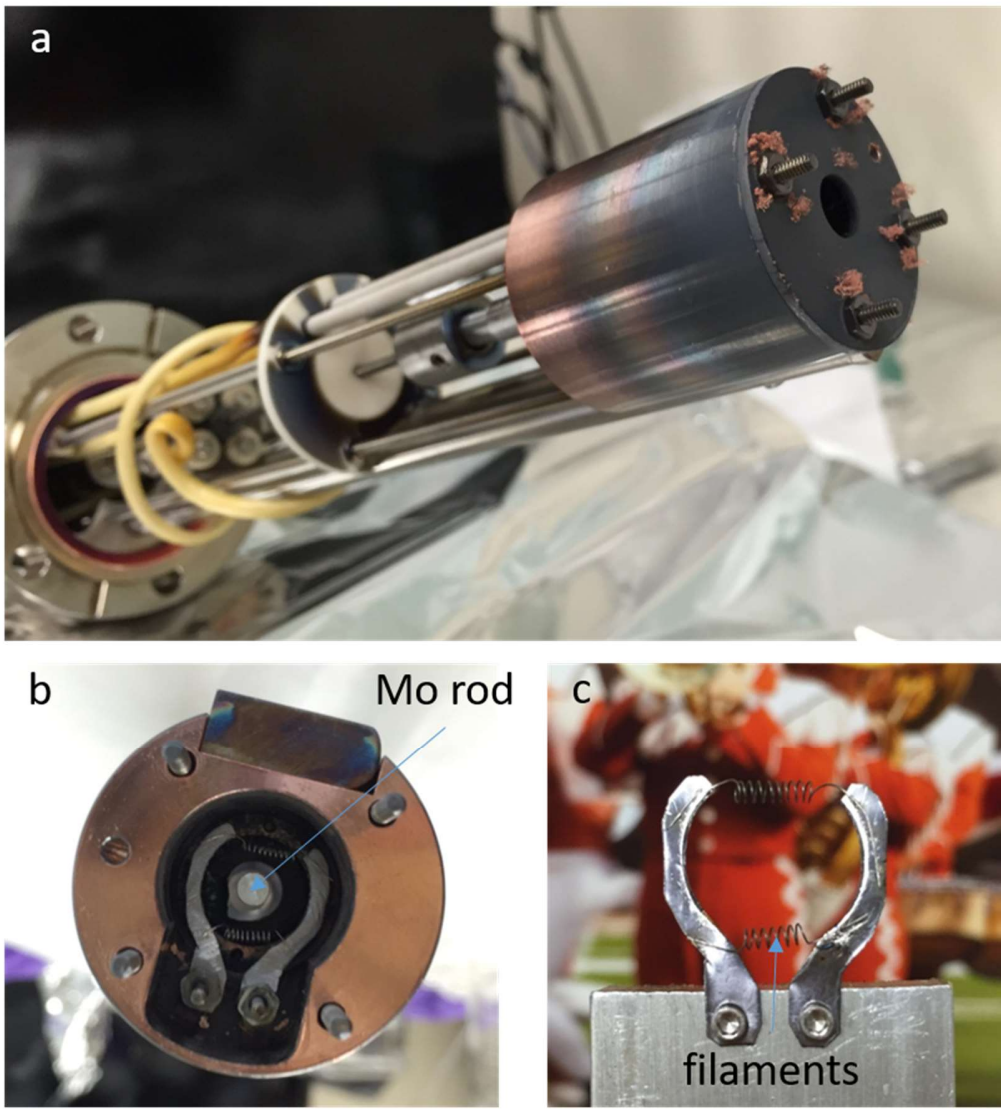

Figure 2.3 Home-built *e*-beam evaporator.

a, The whole assembly. **b**, Top view of the Mo source and the filament. The filament is slightly above the rod. **c**, Spot welded W filaments between Ta half rings, assembled on the fixture for holding them securely.

The structure of our home-built *e*-beam evaporator is illustrated in Figure 2.3, which was reverse-engineered and simplified from a commercial Mantis 4-pocket *e*-beam evaporator. A high voltage of 1500V to 3000V is applied to the high-purity source metal

rod in the middle, and electrons from the hot filaments slightly above the rod are emitted and accelerated toward the rod and transfer the electrical potential energy eventually into heat, which only cause the topmost part of the rod to evaporate. The elegant design allows the two filaments to be very close to the source, as well as clear off the mass flow beam towards the sample. The radiation from the filaments is shielded by the water-cooled copper block surrounding the filaments and the source rod. Molybdenum has been successfully evaporated using such an e-beam evaporator. A second one is being prepared for evaporating Niobium, which is also refractory metal. For Tungsten, which needs to be heated to a much higher temperature, may require a more effective cooling design.

2.3 HEATING STAGE

A stable and controllable substrate temperature is crucial to MBE growth. A radiation heating is applied in the home-built Selenide MBE system, instead of the most commonly used Si-based direct heating mechanism.

For heavily doped Si substrate, directly passing current through the substrate is used for heating, but it is difficult to control the temperature precisely, since a tiny unnoticeable change in current may result in a large notable change in substrate temperature. What's more, the current-to-temperature relation may not be reproducible for different substrates, because the substrates may not be cut into exactly the same dimensions. (These were the reason for my unsuccessful attempt to grow high-quality Bi_2Se_3 films.)

A very simple and concise radiation heating design has been developed for my MBE system, based on the existing direct heating design, as shown in Fig. 2.4. This design is essentially the same as other Si sample stages, except for the three filaments in parallel electrically. Therefore, this design is compatible with all sample holders, of the Omicron design. On each side of the sample holder slot, there are three 0-80 tapped holes for

attaching sample-holding foils. These tapped holes are employed to also hold the tungsten filaments, which are hooked on but electrically isolated from the threaded rods screwed into the tapped holes. The isolation is realized by sandwiching the hooked end of a filament together with a Moly piece in between two 0-80 ceramic shoulder washers. On each side of the sample, the three electric isolation are done using only one piece of Moly, therefore the three filaments are in parallel, and the electrical connection is most simplified. As one can see from Fig. 2.4, the filaments are very close to the sample holder, enabling high heating efficiency. The highest temperature measured on this stage is around 800°C.

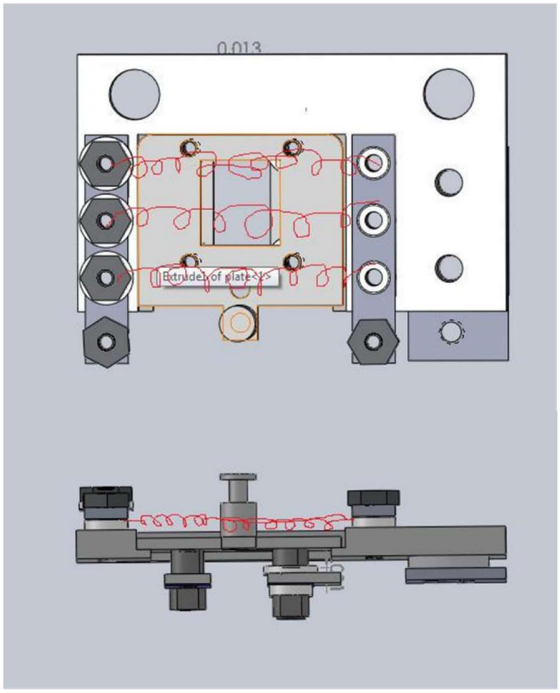

Figure 2.4 Heating stage, top view and side view.

Filaments are hand drawing in red. An Omicron style sample holder is included. Three filaments are placed above the sample holder. They are electrically in parallel. There is a thin Mo foil shielding outside the actually stage.

2.4 RHEED

RHEED is a powerful characterization tool, which is used to monitor the MBE growth in real time. A very brief explanation of the mechanism is in Fig. 2.5, while detailed principles and quantitative analysis of RHEED can be found in the textbook by Ichiyima and Cohen[28].

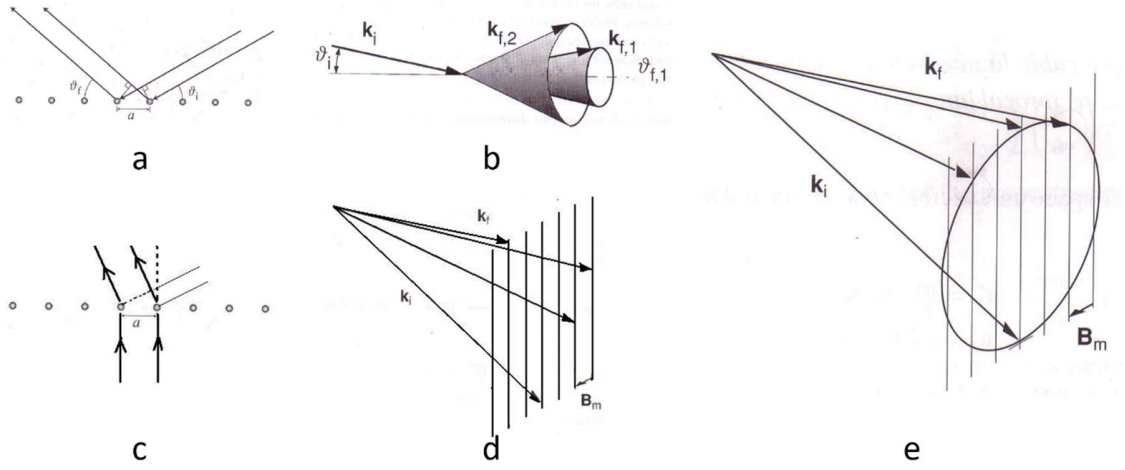

Figure 2.5 Illustration of RHEED mechanism.

a,b, Diffraction from a 1D atomic chain when the incident beam is at a very small glancing angle from the chain. The diffraction direction are in discrete cones. **c,d**, Diffraction from a 1D atomic chain when the incident beam is perpendicular to the chain. The diffraction directions are in discrete parallel lines. **e**, Diffraction from a 2D atomic atomic array in the RHEED geometry, which is the combination of the previous two cases. The diffraction directions are the intersection points of the cones and the lines.

In the geometry of RHEED setup, incident electron beam has a very small glancing angle from the sample surface, usually ~ 2°. Such setup can be viewed as the superposition of the diffraction from two sets of 1D atomic chains, one almost in the same direction as the incident beam, and the other one perpendicular to the beam. As a result, the diffraction directions are the intersect of the diffraction patterns from the two 1D cases. As shown in Fig 2.5e, the RHEED pattern from a crystalline surface is a series of spots falling on a few concentric rings.

In the business of MBE growth, however, the most common RHEED pattern are streaks, or elongated spots, instead of sharp spherical tiny spots. This is due to the finite size effect. The diffraction spots are going to have finite width in both directions, instead of dimensionless ideal spots, and the width, or the angular size of a spot is proportional to the inverse the finite size of the islands. To be specific to RHEED, a 2D island can be projected to a plain perpendicular to the incident electron beam. After the projection, the atomic chain perpendicular to the beam, case c,d in Fig. 2.5, is the same as the original chain, but the other chain, case a,b in Fig. 2.5, is squeezed significantly. As a result, the finite size of the diffraction spot in the vertical direction is significantly larger than the size in the horizontal direction, making the spot elongated or even like streaks. Figure 2.6 illustrates the finite size effect on the RHEED pattern.

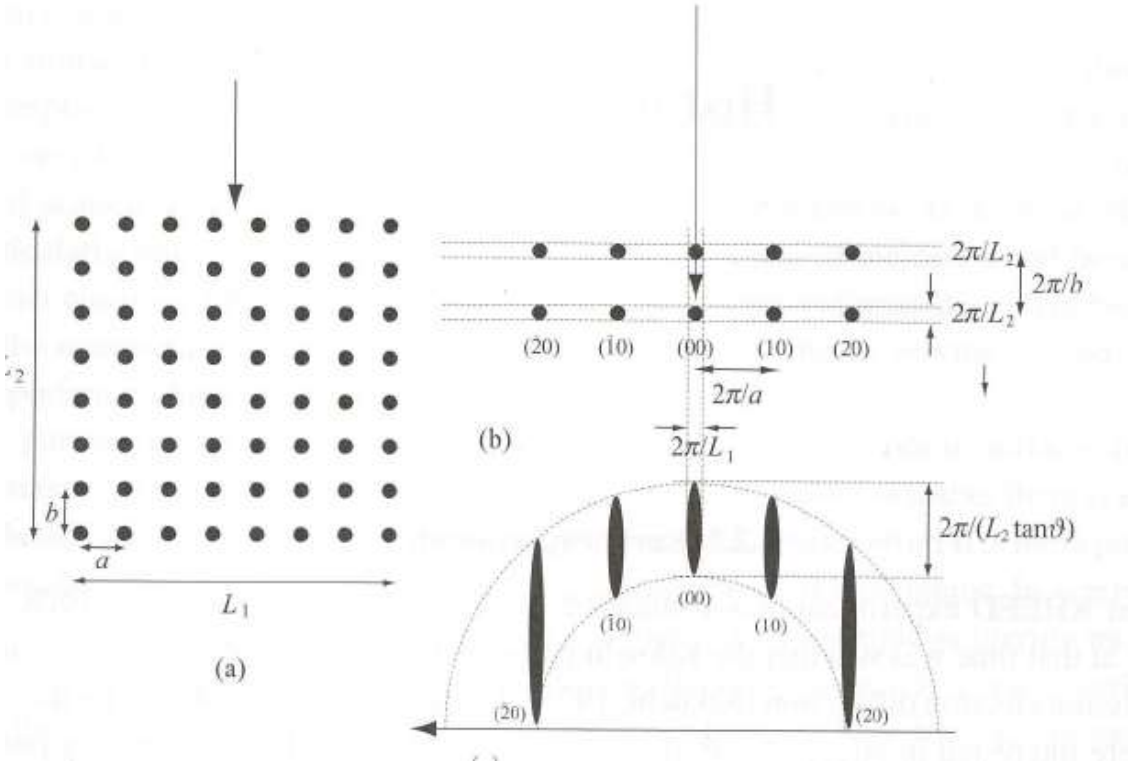

Figure 2.6 Illustration of finite size effect.

2.4.1 Diffraction patterns

The spotty and elongated RHEED pattern have both been observed, and both can be used to calculate the lattice constants of the sample.

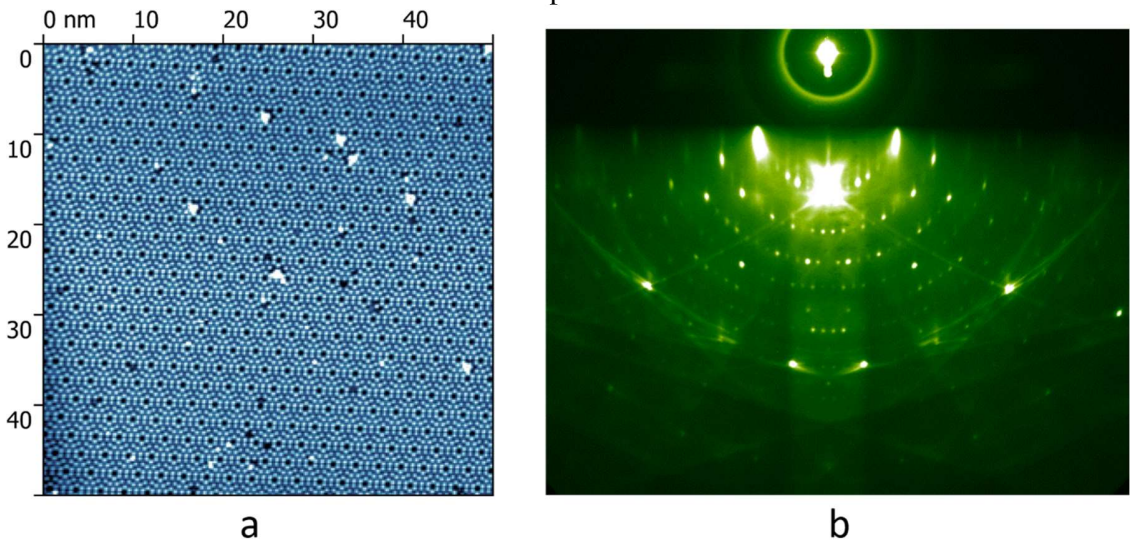

Figure 2.7 Si(111) 7×7 reconstruction surface and its RHEED pattern.

a, 50nm × 50nm STM topography image of Si(111) 7×7 surface. V_{bias} = 2.5 V, I_{tunnel} = 5pA. **b**, RHEED pattern of Si(111) 7×7. Beam energy E = 15 keV. Incident direction is $<11\bar{2}>$. The emission current and camera exposure time was tuned to optimize the image.

For a perfect 2D lattice like Si(111) 7×7 reconstruction pattern, for instance, the corresponding RHEED pattern is featured by sharp spots, as shown in Fig. 2.7. Figure 2.8 shows the evolution of RHEED pattern during the MBE growth of Bi_2Se_3, a layered narrow-gap semiconductor, known as a topological insulator. Eventually the RHEED pattern is streaky for the Bi_2Se_3 film (the bottom panel), instead of spotty, because the MBE grown film has finite island sizes. Quantitatively the lattice constant of the grown sample can be calculated by comparing the RHEED pattern of the sample to the RHEED pattern of a known structure.

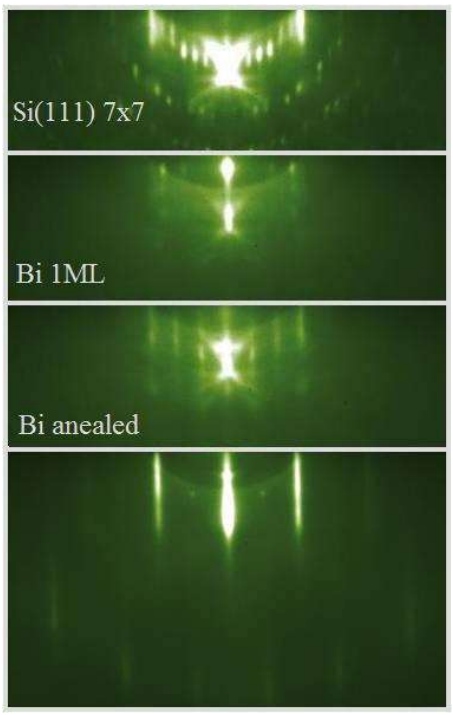

Figure 2.8 RHEED pattern evolution during MBE growth of Bi_2Se_3.

2.4.2 RHEED Intensity Oscillation

Besides using the RHEED pattern to determine the crystal structure of the films, one can also get a relative degree of long range order from RHEED intensity. In principle, RHEED electron beam intensity of a certain spot or streak reflects the long range order of the film, or more plainly, it reflects how flat the film is. If during the MBE growth the sample surface undergoes flat-rough-flat-rough cycles, then the RHEED intensity will also show strong-weak-strong-weak oscillation. Indeed, the MBE process in atomic level has different mechanisms. When the MBE growth is 2D growth initiated by nucleation, instead of 2D step-flow growth initiating from the substrate steps, RHEED intensity has maxima when the growth completes a layer and becomes flat, and has minima when nucleation

cores or small islands cover the surface. The film thickness can be determined by simply counting the number of oscillation peaks. A typical RHEED oscillation is shown in Fig. 2.7, which indicates that the film thickness is 9.5 quintuple layers (a quintuple layer is the basic building unit of layered material Bi_2Se_3)

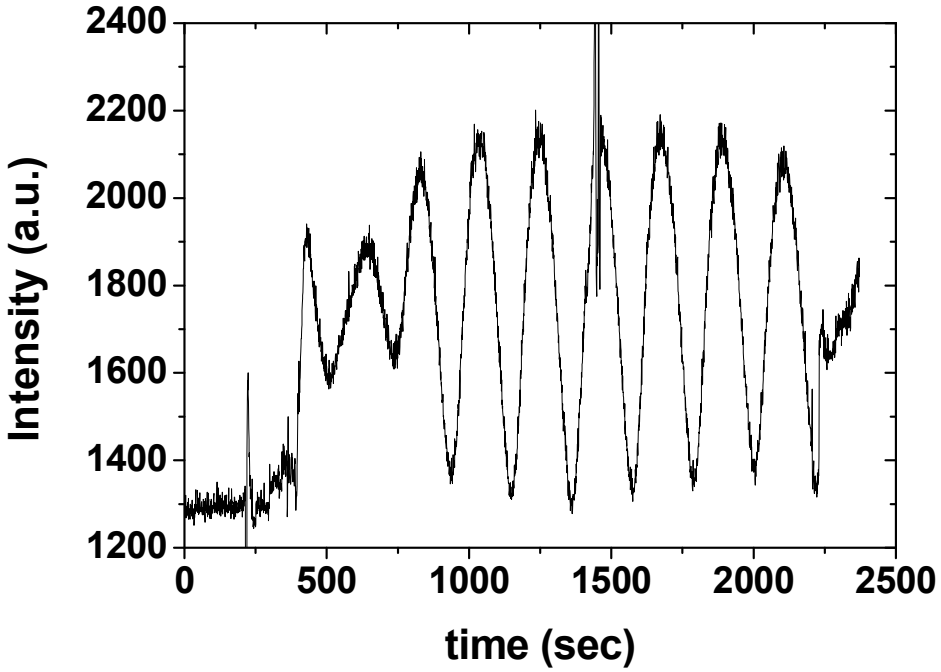

Figure 2.9 RHEED intensity oscillation of Bi_2Se_3 growth.

2.5 CONCLUSION

In conclusion, a home-built MBE system has been designed, built and put into operation. The engineering drawing and the picture of the actual picture of the MBE system is shown in Fig. 2.8. The material synthesized from this MBE includes topological insulators, semiconducting TMDs, and 2D superconductor FeSe, all of which are interesting systems.

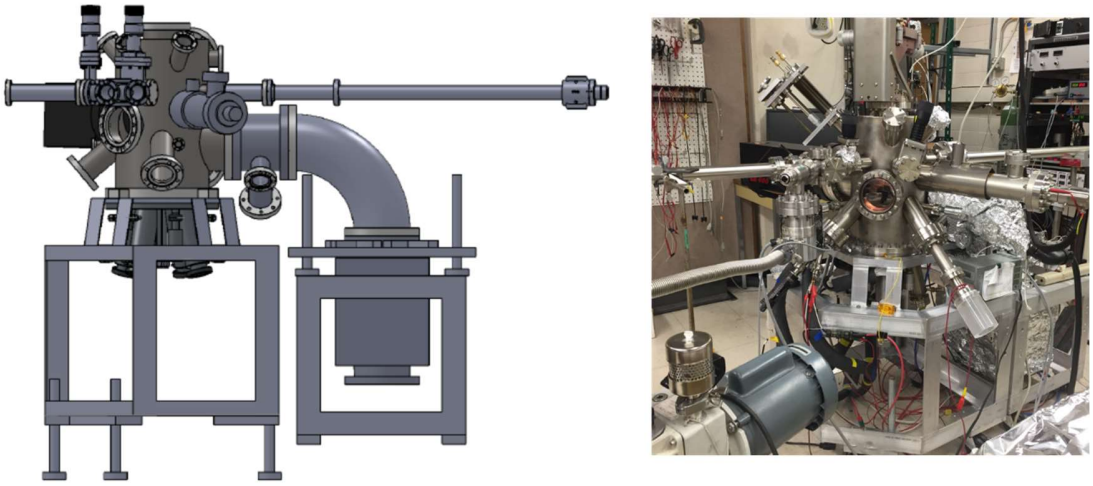

Figure 2.10 Assembly drawing and the actual photo of the MBE system.

Chapter 3: $MoSe_2$ 2D islands

3.1 MBE Growth

The MBE growth of $MoSe_2$ eventually succeeded after a thorough exploration of the growth parameter space. Selenium is supplied much more than the stoichiometry requirement, similar to the case of overdosed As in GaAs growth. There are two reasons: (1) Se's vapor pressure is low and on hot substrates the re-evaporation rate is high; (2) selenium tends to come out of the effusion cell in forms of molecules instead of atoms, reducing the amount of collisions between Se and the substrate. The Se:Mo ratio used in my experiments was 10:1. At the very beginning when a relatively low substrate temperature (~ 400) was applied, the morphology of the as-grown clusters is fractal, which indicates the substrate temperature was too low[29]. As substrate temperature increases, the islands become triangular, hexagonal, and other compact shapes. The optimized temperature for 2D compact islands growth is 550˚C ~ 590˚C. The temperature-dependent morphology is shown in Fig. 3.1. When temperature increases even higher, the compact islands become more isotropic.

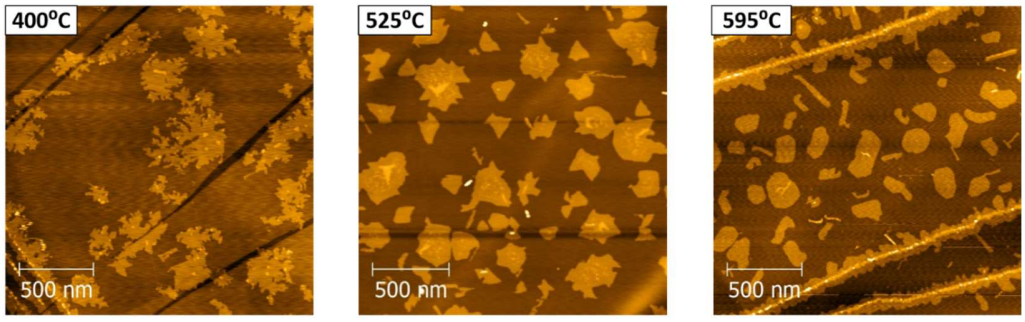

Figure 3.1 Temperature-dependent island morphology of $MoSe_2$.

The RHEED patterns before and after the MBE growth for the sample in Fig. 3.1b are presented in Fig. 3.2**a** and **b**, respectively. The uniform streaks in **b** confirmed the successful growth of crystalline $MoSe_2$ films. Quantitatively, the distance between streaks is proportional to the inverse of the lattice constant. By assuming the HOPG lattice is the commonly accepted value 2.46Å, one can calculate the lattice constant corresponding to the pattern in Fig. 3.2b to be 3.27Å, which is in perfect agreement with other reports of the lattice constant of $MoSe_2$. Such agreement also indicates that the zigzag directions of the MBE grown $MoSe_2$ film follow the zigzag directions of the underlying HOPG, otherwise there should be a factor of $\sqrt{3}$ involved. Therefore, although the weak vdW interaction reliefs the lattice-matching requirement for epitaxial growth, the MBE $MoSe_2$ films still prefer certain orientations, in contrast to the randomly oriented CVD samples.

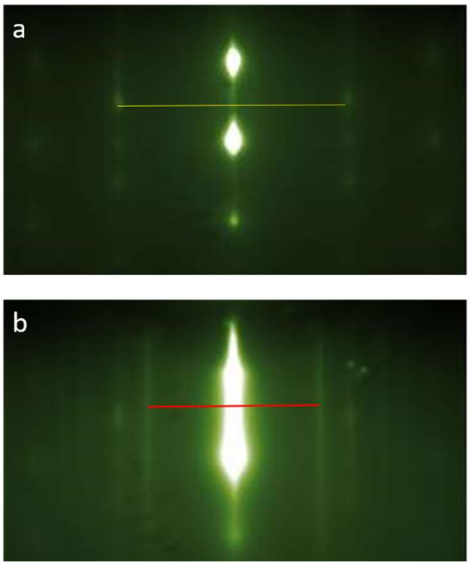

Figure 3.2 RHEED patterns before and after MBE growth of $MoSe_2$.

3.2 STM/STS STUDIES

3.2.1 STM topography of $MoSe_2$

A typical compact $MoSe_2$ island is shown in Fig 3.3. Fig 3.3a and c were plotted in false color scale. The warmer the color is, the higher the surface is. The dark blue regions are the HOPG substrate. The green area is ML $MoSe_2$, and the two hexagons are BL $MoSe_2$. The bright (yellow) straight lines on ML (green) area are domain boundaries. It is evident that the single-domain areas all have triangular or hexagonal shapes. Fig 3.3b is the height profile along the red dashed line in Fig 3.3a. The layer thickness is ~ 0.7 nm, in good agreement with the value in Chapter 1.

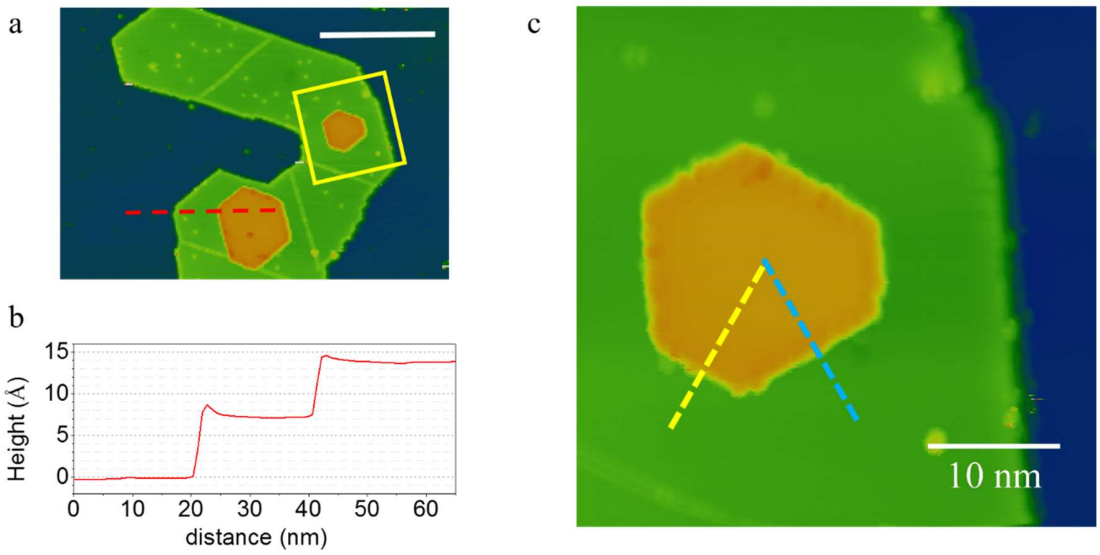

Figure 3.3 STM topography of a compact 2D island.

a, 175nm × 120nm STM topography image. Blue, green, and orange regions are HOPG, ML and BL $MoSe_2$, respectively. The white scale bar represents 50nm. **b**, Height profile along the red dashed line in **a**. The thickness of a ML $MoSe_2$ is ~ 7 Å. **c**, Zoom-in image (40nm × 40nm) of the hexagonal 2nd-layer area highlighted in **a**. All STM data were taken with sample bias V = -2V and tunneling current I = 5 pA.

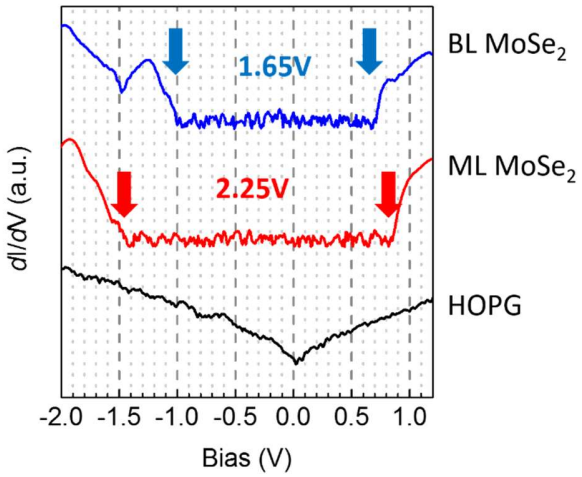

Figure 3.4 *d*I/*d*V spectra of HOPG, ML and BL $MoSe_2$ in logarithm scale, stacked with an offset.

Fixed-separation differential conductance dI/dV spectra (introduced in **Appendix D**) were taken on HOPG, ML and BL $MoSe_2$, as shown in Fig 3.4. Tip was stabilized at V = -2.0V and I_{tunnel} = 25pA. There is obvious shifting in the conduction band minima (CBM) and in the valance band maxima (VBM) of ML and BL $MoSe_2$. ML band gap of $MoSe_2$ is 2.25eV, and the BL gap is 1.65eV. The band gap values from my STM are also in good agreement with others.

The bandgap and the morphology of the islands actually contains a lot more information. ML $MoSe_2$ has two crystal structures: 1H and 1T[30], which has distinct electronics structures. The bandgap measured here suggests that, the crystal structure of the MBE grown $MoSe_2$ on HOPG is 1H. Moreover, 1H structure has two different zigzag edges, but only one kind of arm-chair edge. From the unequal edges of the hexagonal BLs, one can infer that the edges are of zigzag type. It is believed that, the long edges of the hexagons are Mo-terminated zigzag edges, while the short ones are the Se-terminated zigzag edges.

3.2.2 ML-BL lateral heterojunctions

The hexagonal BL regions have a distinct electronic structure from the surrounding ML region, as evidently shown in Fig. 3.4, therefore such a ML-BL junction is a natural lateral hetero-junction (LHJ). In this section I present the band bending and alignment across such LHJs measured with STM/STS. (Similar results have been reported in[31] from our group.)

Constant-current dI/dV spectra were taken on a series of points along the yellow and blue dashed lines in Fig. 3.3c. Each individual dI/dV spectrum, similar to the curves in Fig. 3.4, can be color coded and displayed vertically. The vertical color-coded spectrum stripes can then be arranged in a row to visualize the spatial variation of the band structure. Such imaging technique will be referred to as dI/dV mapping throughout this dissertation. The dI/dV mapping along the yellow and the blue dashed lines are shown in Figure 3.5.

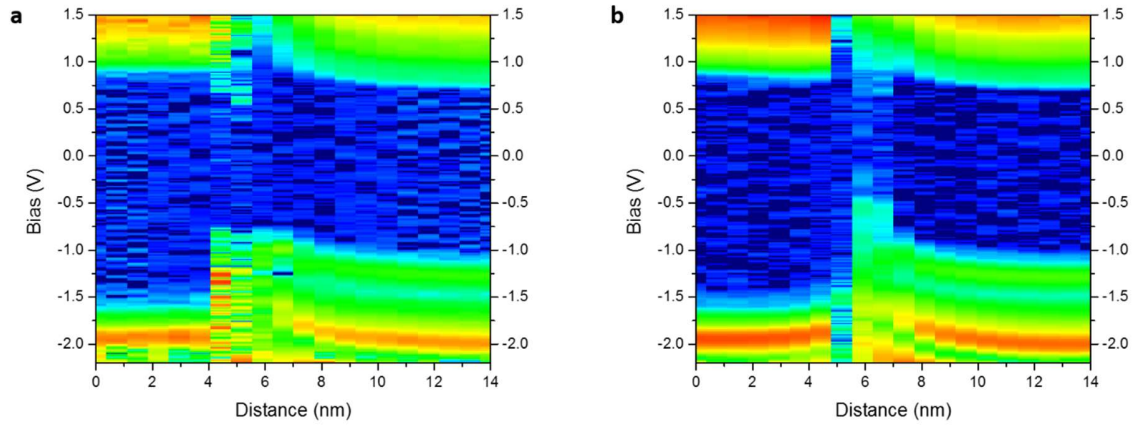

Figure 3.5 dI/dV mapping across different BL edges.

a, Across a short edge (along the yellow dashed line in Fig. 3.2c). **b**, Across a long edge (along the blue dashed line in Fig. 3.2c). Each mapping contains 20 equally spaced sampling points, with ~0.7nm apart. The current setpoint was 25pA, and the bias sweep was from -2.2V to +1.5V.

The electronic structures of the two edges have obvious difference. The short edge has an obvious gap comparable to the BL gap, and the gap states are only below the CBM. The long edge, on the other hand, has a much smaller and less obvious gap, and the edge states are mostly above VBM. The difference probably stems from the different edge terminations.

In conclusion, $MoSe_2$ thin films have been successfully grown using MBE. The bandgap reduction from ML to BL is clearly manifested in the ML-BL lateral heterojunction.

Chapter 4: $MoSe_2$ nanoribbons

During the early practice of MBE growth of $MoSe_2$ on HOPG, nanoribbons could already be occasionally observed. Inspired by the achievements on graphene nanoribbons, I decided to try the controllable growth of $MoSe_2$ nanoribbons. The exploration of the MBE growth parameter space has turned out to be fruitful. I managed to grow $MoSe_2$ nanoribbons at relatively high substrate temperature. At the same time, I discovered an unexpected three-stage morphological phase transition of $MoSe_2$ growth: from fractal to compact, and eventually to elongated shapes, in stark contrast to the long established fractal-to-compact two-stage growth mode transition. By cooperating with theorists from the University of Science and Technology of China (USTC), I discovered the critical role that Se:Mo ratio played during the nanoribbon growth experimentally. Meanwhile, first-principles calculations from USTC discussed the edge reconstruction and relative edge energies in both Se-abundant and Se-deficient conditions and successfully explained the growth mechanism of $MoSe_2$ nanoribbons. Our corroborative efforts are reported in the article "Controlled fabrication of $MoSe_2$ nanoribbons via an unexpected morphological phase transition", which has been submitted and is being reviewed by editors.

4.1 BACKGROUND

4.1.1 Graphene nanoribbons

As the first and arguably most important member of the two-dimensional (2D) materials family, pristine graphene possesses exotic intrinsic properties[1,32–34], and properly tailored graphene nanostructures are further expected to exhibit various emergent properties of potential technological significance[35–38]. One compelling example is

graphene nanoribbons (GNRs), which may develop tunable bandgaps[39,40], support robust edge states[41], and display half-metallicity under an external electrical bias[42]. For these very reasons, various innovative methods have been developed to achieve controlled fabrication of GNRs, including both bottom-up[35,43–46] and top-down[40,47–49] approaches, enabling the revelation of rich and intriguing physical phenomena[50–52]. A few fabrication techniques of GNR are show below:

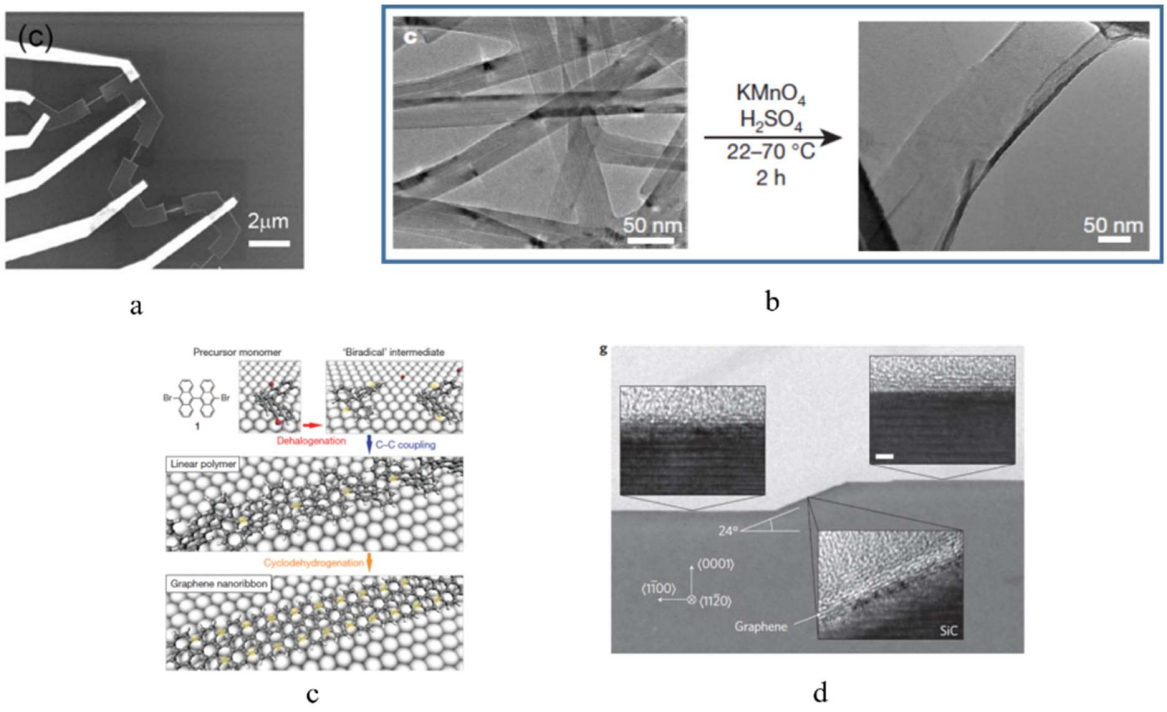

Figure 4.1 A few examples of GNR fabrication techniques.

a, Electron beam lithography[40]. Nanoribbons are the short thin connections between the dark belts. The bright white areas are metal electrodes. **b**, unzipping of carbon nanotube[49]. **c**, Schematic of GNR self-assembly[44] from molecules. **d**, Epitaxial growth on etched SiC facet[45]. **a, b** are top-down approaches; **c, d** are bottom-up approaches.

4.1.2 TMD nanoribbons

Beyond graphene, transition metal dichalcogenide (TMD) materials have emerged as another important class of 2D systems with inherently different physical properties, most notably the existence of intrinsic bandgaps[5,21,26] and much stronger spin-orbit and spin-valley coupling effects[30,53,54]. When reduced to nanoribbon geometries, the very compound nature of the TMD systems further introduces complexities compared with their graphene counterparts. To date, only limited successes have been demonstrated in the fabrication of TMD nanoribbons using top-down approaches[55,56], shown in Fig. 4.2. The top-down lithography technique using transmission electron microscopy (TEM) electron beams has its limitations, in the sense that, (1) the high energy electrons could change the chemical stoichiometry of the TMD compound, and (2) the as-prepared nanoribbons will be on a TEM grid and hard for follow-up studies. Thus, a viable bottom-up approach for controlled mass production of high-quality TMD nanoribbons remains to be discovered. This standing obstacle severely hinders potential advances in exploring their exotic electronic[57], magnetic[58,59], optical[10,60], and catalytic[61] properties for device applications.

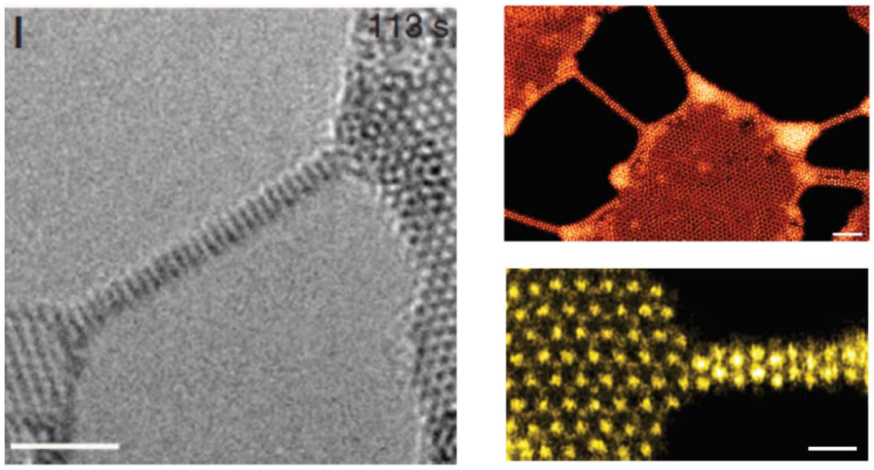

Figure 4.2: Top-down approaches of creating TMD nanoribbons.

The **left** panel is by Liu, X., *et.al.*[55]; **Upper** and **lower right** panels are by Lin, J.,*et.al.*[56]

4.2 NANORIBBON GROWTH AND CHARACTERIZATION

4.2.1 Temperature-dependent MBE growth

Monolayer (ML) $MoSe_2$ has been successfully grown using MBE on various vdW substrates[25, 16,17,31,62]. Our MBE growth of $MoSe_2$ on highly oriented pyrolytic graphite (HOPG) could take place over a large range of substrate temperature (T_{sub}), and the morphology of the $MoSe_2$ flakes shows strong T_{sub} dependence. Figure 3.3 shows a sequence of ambient atomic force microscopy (AFM) images of $MoSe_2$ grown at different T_{sub} but at a fixed nominal Se:Mo flux ratio of 10:1. At T_{sub} < 500˚C, the $MoSe_2$ flakes have fractal shapes. At an intermediate T_{sub} (between 500˚C and 600˚C), $MoSe_2$ forms 2D compact islands. Many of the compact islands or nanodots are of triangular or hexagonal shapes, with well-defined corners of 60°, 90°, 120°, and 150° (see details in Fig. 4.10), and the underlying growth mechanisms leading to these specific shapes will be discussed later. When the growth temperature rises within this range, the compact islands become more and more isotropic, with increasing numbers of shorter straight edges and more smeared corners. Thus far, this temperature-dependent growth mode can be well understood within the contexts of shape transformations in nonequilibrium growth of surface-based nanostructures[29,63,64].

Strikingly, when T_{sub} gets even higher, a completely different morphology, *nanoribbon*, becomes dominant. As shown in Fig. 4.3g, when T_{sub} = 620˚C, nanoribbons with well-defined orientations become quite evident. As the temperature is raised further (e.g. Fig. 4.3h for T_{sub} = 640˚C), the nanoribbon density becomes much smaller and individual nanoribbons are not as straight as those at 620˚C. At even higher temperatures,

one no longer can observe any growth of $MoSe_2$ at all. The statistical analysis of the size/shape and orientation of a total number of 140 nanoribbons grown at T_{sub} = 620˚C is presented in Fig. 4.4. The width of the nanoribbons matches with a Gaussian distribution, possessing an average value of 17 nm and a standard deviation of 7 nm as shown in Fig. 4.4a. The aspect ratio is most probably between 4 and 14, with exceptions as high as 20. The thickness distribution indicates that the ribbons are mostly ML- and bilayer- (BL-) high, and the ML ribbons, 40 out of 140, have better defined thickness than the BLs. The thickness of ML nanoribbons are shown in detail. The well-defined orientations of the nanoribbons are 60˚ apart, clearly manifesting the three-fold symmetry of the substrate. Such a morphological phase transition from the compact to elongated shape is unusual and unexpected.

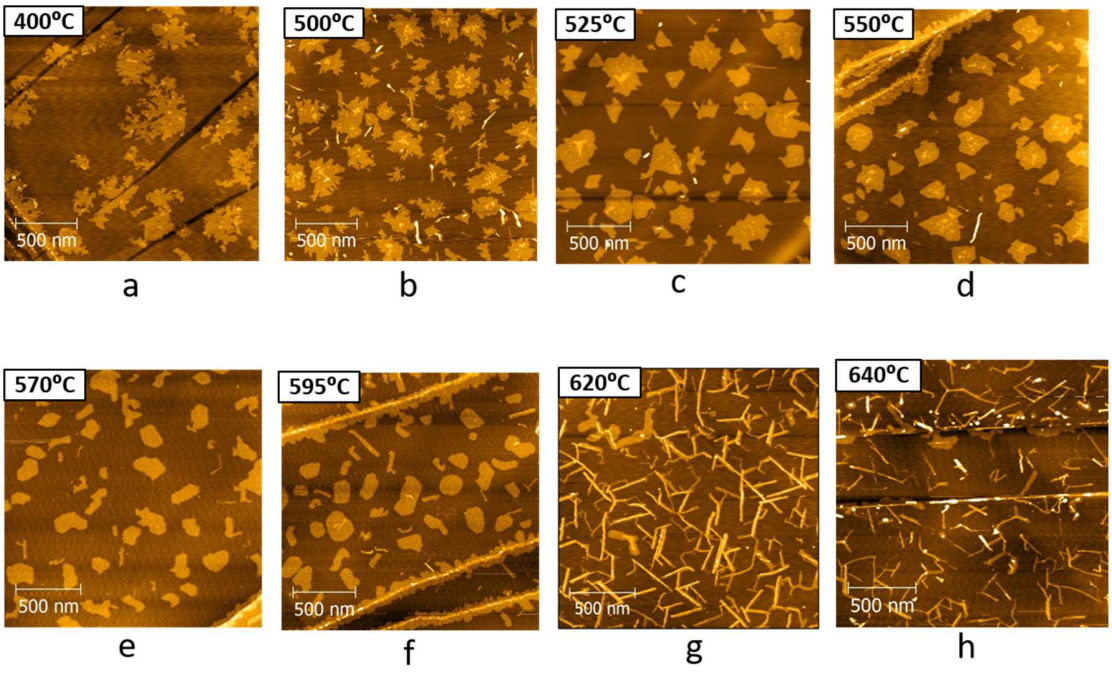

Figure 4.3: Morphological phase transition of $MoSe_2$.

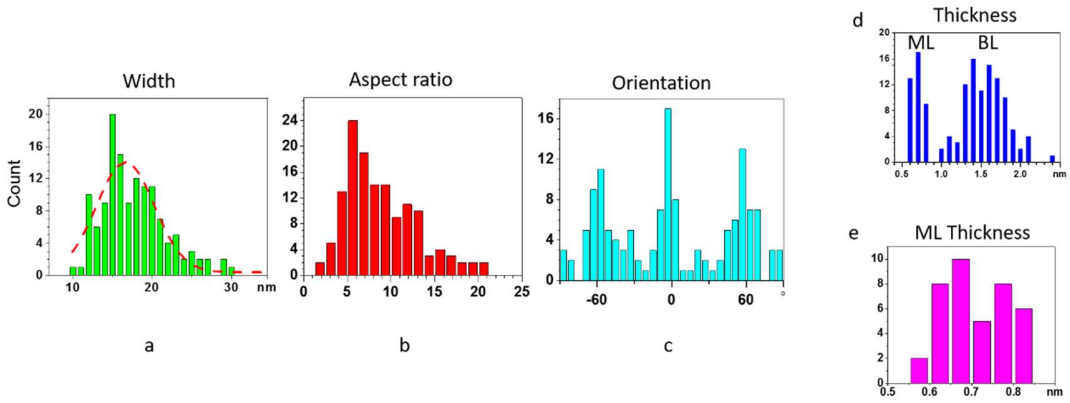

Figure 4.4 Statistical description of the morphology of nanoribbons.

a-d, Width, aspect ratio, orientation, and thickness of all 140 nanoribbons in Fig. 4.3g, respectively. **e,** Thickness of the 40 ML nanoribbons among the 140 total.

4.2.2 TEM characterization of $MoSe_2$ nanoribbons

To identify the morphological nature of the $MoSe_2$ nanoribbons, their atomic and electronic structures have been characterized by both TEM and STM/STS. TEM experiments were carried out by collaborators in Zhejiang Unviersity, China. The $MoSe_2$ samples were covered with ~ 5 nm Se post growth as protection, and then taken out of UHV and shipped. Mild annealing of the sample at about 300 ˚C is required to remove the protecting Se layer. The technical details of TEM is in **Appendix A**. Typical zoom-in views of the nanoribbons are shown in Figs. 4.5a and 5.6a. We notice that one edge of a typical nanoribbon is usually straighter, while the other one contains more kinks. Unlike graphene, TMD nanoribbons within the stable 1H structure have two different types of zigzag (ZZ) edges, one Mo-terminated (ZZ-Mo) and the other Se-terminated (ZZ-Se), but only one type of armchair edge[58](AC). Therefore, the asymmetry of the edge morphology strongly suggests that the long and distinctly different edges of the nanoribbons are zigzag edges.

Indeed, the atomic-resolution images in Fig. 4.5b-c evidently show the honeycomb pattern, which confirms the lattice structure of the $MoSe_2$ nanoribbons to be still the stable 1H phase instead of the metastable 1T or 1T'.[30] This observation implies that there is no structural phase transition accompanying the morphological phase transition, the latter resulting in the formation of the nanoribbons. Moreover, from the atomic registry determined by the brightness of the atoms, it is inferred that the long edges of the ribbons are all zigzag edges, with the straighter edges to be Mo-terminated, while the more kinky edges to be Se-terminated edges. It is also noticed that there are non-crystalline clusters on both the nanoribbons and the substrates. The BL thickness shown in Fig. 4.4d is likely bewildered by such clusters, which cannot be distinguished by the ambient AFM.

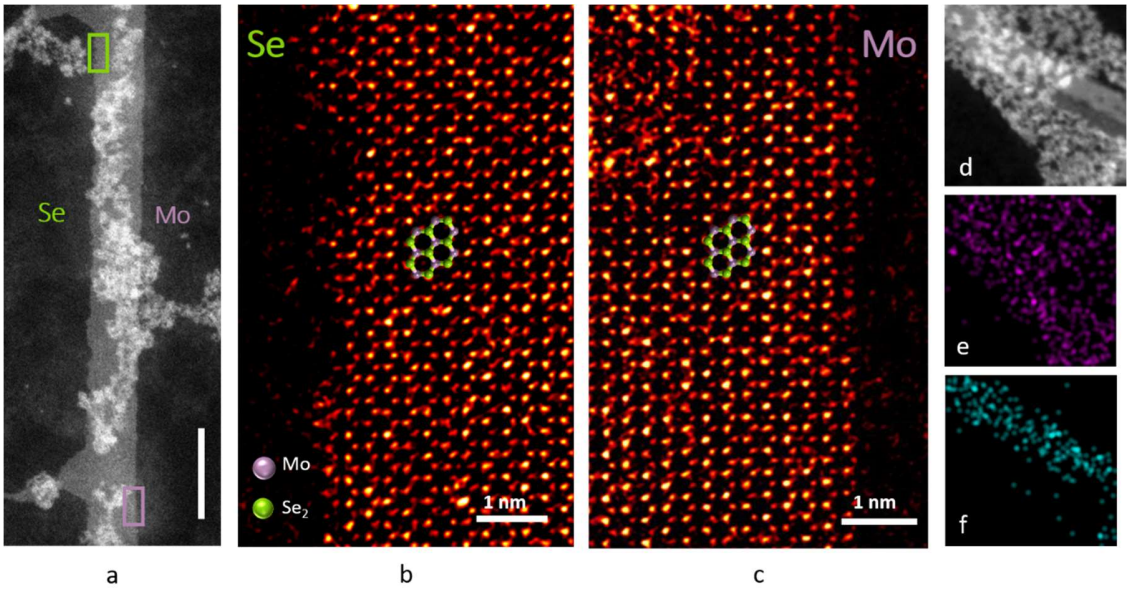

Figure 4.5: TEM and EDX characterization of $MoSe_2$ nanoribbons.

Energy-dispersive X-ray spectroscopy (EDX) has been applied to identify the chemical composition of the clusters, shown in Fig. 4.5d-f. Evidently, the Se signal only

appears in the crystalline nanoribbon area, while the Mo signal appears in both nanoribbon and the cluster. These observations suggest that, during the nanoribbon growth, there were extra Mo atoms on the HOPG surface, despite the nominal Se:Mo ratio that was deliberately kept at 10:1 during growth.

4.2.3 STM/STS characterization of $MoSe_2$ nanoribbons

STM/STS is further utilized to characterize the electronic structure of the $MoSe_2$ nanoribbons. STM topography images again confirm the asymmetry of the edge straightness. Due to the influence of the edges, the electronic structure of the ribbon varies substantially across the ribbon width with respect to the distance to the edges. For a ribbon of average width in Fig. 4.6b, the differential conductance (dI/dV)[15,65,66] mappings across the ribbon are shown in Fig. 4.7c-d. In the core region of the ribbon, the bandgap is the same as that of 2D flakes within the 1H phase[16,17]. This observation once again confirms that there is no structural phase transition in the nanoribbons. Near the edges, the bandgap is significantly narrowed, by different amounts along the two different zigzag edges, likely due to boundary effects and edge reconstructions. From left to right, there are three electronically distinct areas: Se-terminated edge, core, and Mo-terminated edge. It is worthwhile to emphasize that, overall, both the chemical purity and morphological quality of the nanoribbons fabricated here using the bottom-up self-assembly approach are clearly superior to those achieved using the more intrusive top-down approaches of TEM-based cutting of pristine TMD MLs.

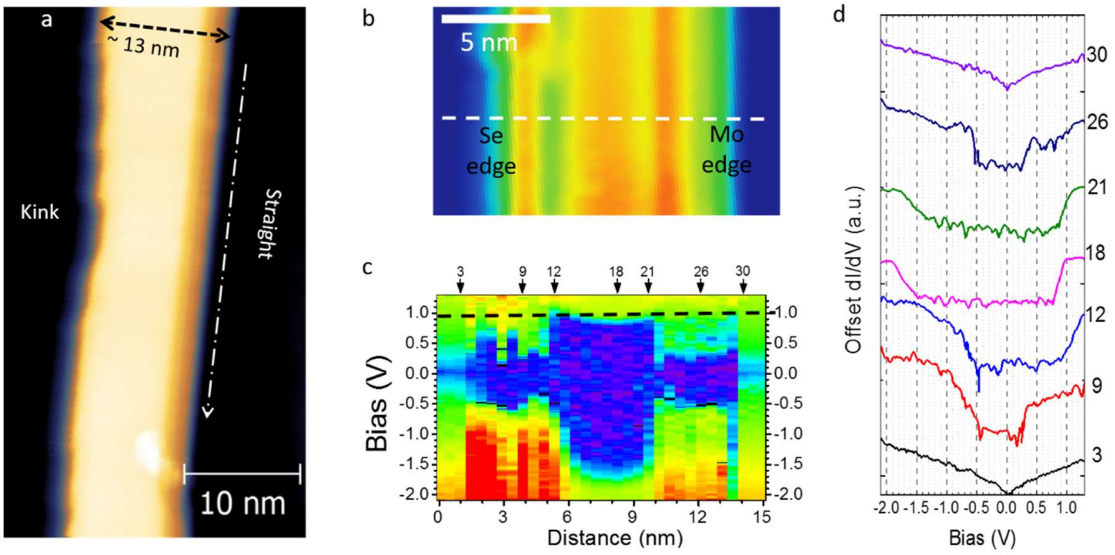

Figure 4.6: Electronic properties of $MoSe_2$ nanoribbons.

a, STM topography image of a nanoribbon, taken at the sample bias of V_b = +3 V and tunnelling current of I_{tunnel} = 10 pA. **b**, STM topography of a nanoribbon segment, taken at V_b = +1.0 V and I_{tunnel} = 5 pA. The left edge has more kinks and is determined to be Se-terminated, while the straighter right edge is Mo-terminated. **c**, Color-scaled d*I*/d*V* mapping across the nanoribbon taken along the white dashed line in **b** with a separation of 0.5 nm between adjacent sampling points. The range of bias sweep is from -2.1 to 1.3 V. The black dashed line is located at +1.0 V, the bias applied in **b**. **d**, Representative individual d*I*/d*V* spectra at some typical areas across the $MoSe_2$ nanoribbon and on the HOPG substrate, as marked by the arrows in **c.**

4.3 UNVEILING THE NANORIBBON GROWTH MECHANISM

4.3.1 Conjecture on the morphological transformation mechanism

In attempting to reveal the likely underlying mechanism for the morphological phase transition from the compact islands to the nanoribbons, we note that, ultimately, the evolution of the island shape is dictated by the relative energetics and growth rates of the different and competing edge structures. If the bonding configurations of the different edges remained the same during growth, a higher temperature would only lead to islands

with more isotropic shapes. The growth behaviour in the sequence from Fig. 4.3c-f indeed follows this expectation. Then what causes the dramatic transformation from the compact 2D islands to the nanoribbons at 620 ˚C? The most probable reason is that *the relative energetics and growth rates between the different edges have been altered at the transition temperature*.

Here we recall that MBE growth of $MoSe_2$ needs to be carried out under a high Se:Mo flux ratio in order to keep Se atoms available on the surface for growth (with super-saturated Se due to its high vapor pressure). At a constant Se flux, a higher substrate temperature would actually imply a lower concentration of available Se adatoms at the growth front of the 2D islands. EDX results in Fig. 4.5d-f even imply that the actual amount of Se was insufficient to react with all the Mo atoms on the HOPG surface. We therefore conjecture that the available Se concentration on the surface must have played a crucial role in modifying the bonding configurations of different edge structures and thus altering their relative energetics and growth rates. In the following, this conjecture is further investigated both experimentally and theoretically.

4.3.2 Experimental validation of the conjecture

We now independently control the Se:Mo flux ratio, and compare the new growth mode with the earlier one. It is evident that the transition temperature from the 2D (or compact) to 1D (or elongated) growth mode can indeed be altered by the nominal Se:Mo flux ratio. At 570 ˚C, which fell into the 2D compact growth regime earlier (Fig. 4.7a), nanoribbons can now also form when the Se pressure is lowered by half, to Se:Mo=5:1 (Fig. 4.7c). Furthermore, at 620 ˚C, which fell into the nanoribbon growth regime earlier (Fig. 4.7b), 2D compact islands now become the dominant morphology when the Se pressure is doubled, to Se:Mo=20:1 (Fig. 4.7d). These definitive observations

corroboratively verify the important role of Se adatoms in triggering the dramatic morphological transformation, favouring nanoribbon growth at lower Se concentrations.

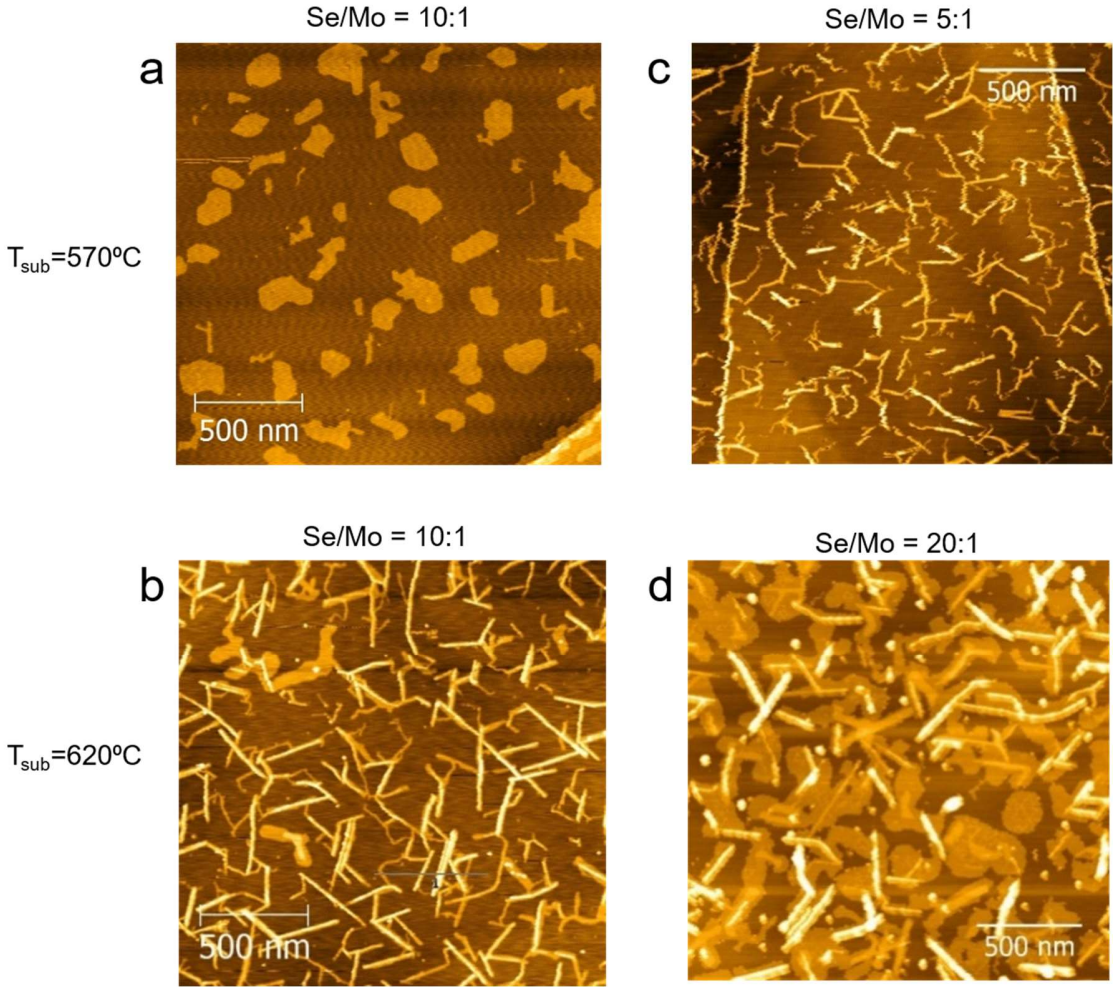

Figure 4.7 Se:Mo-ratio-controlled morphological phase transition.

a,**b**, Same AFM images of $MoSe_2$ at the Se:Mo flux ratio of 10:1 as Fig. 4.3e and 4.3g, respectively. **c**, AFM image of $MoSe_2$ grown at the same T_{sub} as in **a**, but with the Se:Mo flux ratio reduced by one half to 5:1. **d**, AFM image of $MoSe_2$ grown at the same T_{sub} as in **b**, but with the Se:Mo flux ratio doubled to 20:1.

4.3.3 Atomistic growth mechanism from first-principles calculations

To gain further insights into the atomistic growth mechanisms of the nanoribbons, we use first-principles calculations within density functional theory (DFT) (see **Appendix B** for details) to compare the energetics of the zigzag and armchair nanoribbons under the Se-poor and Se-rich conditions. In either case, we model the zigzag or armchair nanoribbons with supercells that contain the same numbers of Mo and Se atoms, allowing direct comparison of their relative stability by their total energy difference. As illustrated in Fig. 4.8a-b under the Se-poor condition defined by unpassivated Mo-terminated edges, a global (2x1) reconstruction along both the Mo- and Se-terminated edges occurs for the zigzag nanoribbons, while the edge Mo and Se atoms tend to shift only slightly for the armchair nanoribbons. For the zigzag nanoribbon, the dramatic (2x1) reconstruction along the Mo-terminated edge is via place exchange, with substantial inward displacements of all the first-row Mo atoms and corresponding outward displacements of half of the second-row Se atoms, making the edge Mo atoms all effectively passivated by the displaced Se atoms rather than by extra Se adatoms[59]. The (2x1) reconstruction of the Se-terminated edge is significantly milder than that at the Mo-terminated edge, characterized by slight local place readjustments of the edge atoms. Such reconstructions dramatically reduce the total energy of the zigzag nanoribbon by 0.85 eV per supercell compared to the armchair nanoribbon.

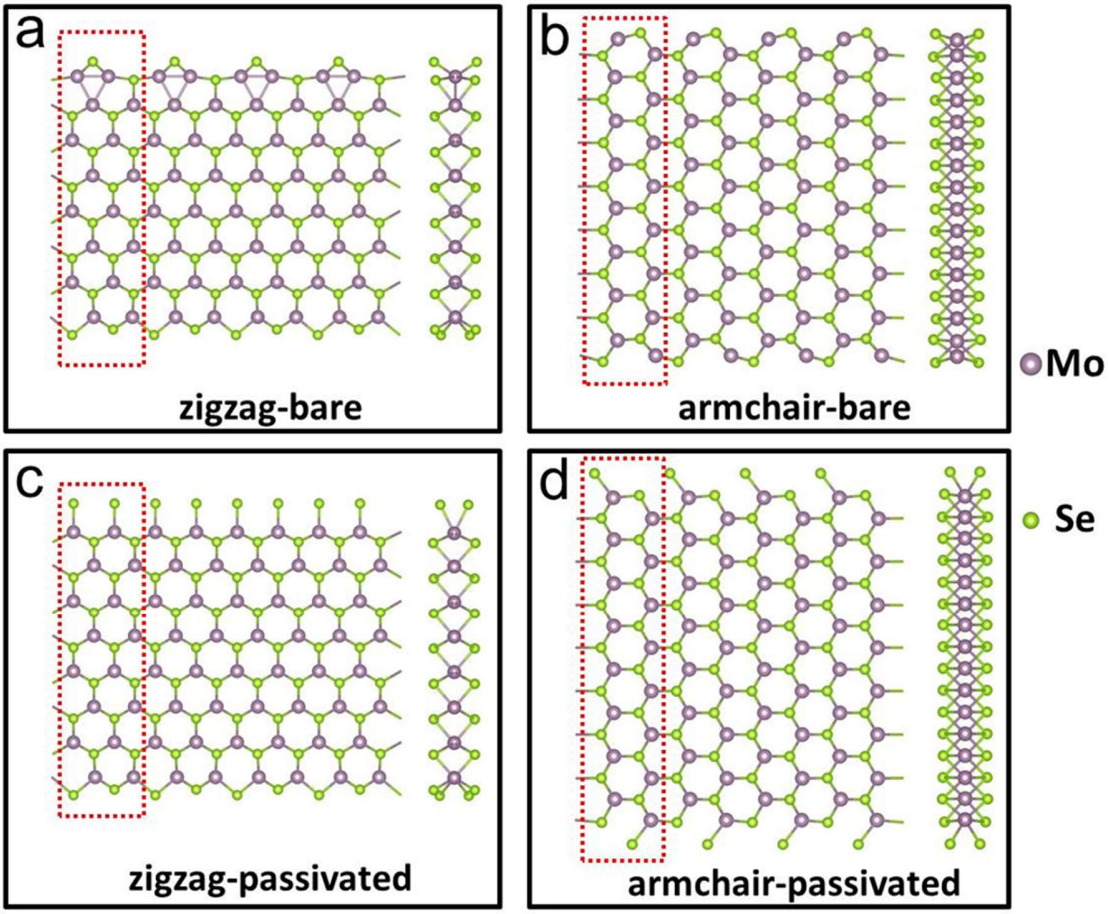

Figure 4.8: Optimized atomic structures and energy differences of different $MoSe_2$ nanoribbons, laid in horizontal direction.

a,**c**, Structures of zigzag nanoribbons without and with extra Se dimers along the edges, respectively. **b**,**d**, The corresponding structures of armchair nanoribbons. Both top and side views are shown for the nanoribbons. The atoms included in the supercell calculations in each case are indicated by the dotted rectangle. The energy difference in the upper case (without extra Se dimer passivation) is 0.85 eV per supercell, while that in the lower case is 0.10 eV per supercell.

Based on DFT, in Se-poor condition the ZZ edges of initial clusters are going to be reconstructed and become stable, or inert. So the growth will happen on the AC edges, and the cluster will extend in the normal directions of the AC edges. At the same time, such growth is also going to create two parallel ZZ edges, perpendicular to each AC growth front. The new ZZ edges are also stable and inert, so growth is only 1D, resulting in

nanoribbons. So, regardless of the shape of initial clusters, in Se-poor condition, nanoribbons should be the prevalent morphology. For the particular nanoribbon in Fig. 4.5a, with a triangular extrusion, its growth mechanism is illustrated in Fig. 4.9.

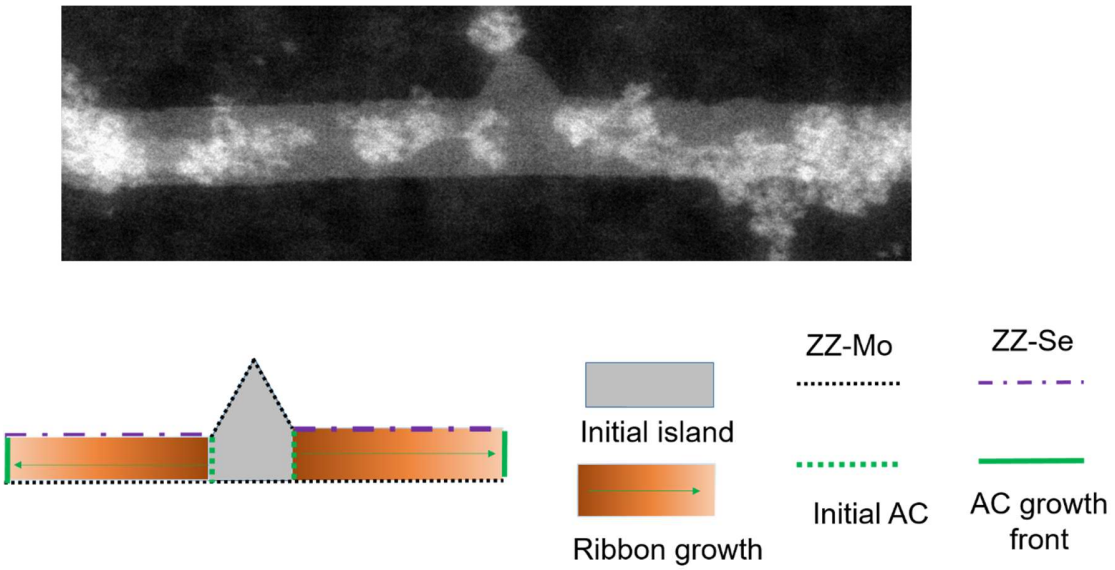

Figure 4.9: Ribbon growth initiated from a triangular cluster.

The **upper** panel is the same nanoribbon shown in Fig. 4.5a, which has a triangular extrusion. The **lower left** panel is schematic of the edges assignment and the growth mechanism of the nanoribbon. The **lower right** panel are legends. ZZ-Mo, ZZ-Se, and AC are abbreviations for Mo-terminated zigzag edge, Se-terminated zigzag edge, and armchair edge, respectively.

Within this growth mechanism, the two edges of the $MoSe_2$ nanoribbons should be the two different zigzag edges, i.e., Mo-terminated edge and Se-terminated edge, which have been confirmed by the TEM images of the nanoribbon shown in Fig. 4.5b-c. Our DFT calculations also show that the energy gain along the reconstructed Mo-terminated edge is 0.82 eV per formula unit relative to the unreconstructed case, while the energy gain for the

reconstructed Se-terminated edge is 0.16 eV per formula unit. The distinct energy difference should provide an important basis for differentiating such edges in the experiments. In particular, the more stably reconstructed Mo-terminated edge becomes straighter, while the less stable Se-terminated edge contains more kinks, as displayed in Fig. 4.5a and Fig. 4.6a.

In contrast, under the Se-rich condition the excess Se adatoms can effectively passivate the edge Mo atoms. Figure 4.8c-d shows the structures of the zigzag and armchair nanoribbons with an extra Se dimer added at each edge Mo atom, while the inner atoms essentially keep their respective bulk-terminated positions. The total energies of the fully passivated zigzag and armchair nanoribbons are found to be much closer, with the former lower by only 0.10 eV per the large supercell. In this case, the growth rates of the zigzag and armchair edges are also expected to be nearly the same, thereby favoring compact structures of the $MoSe_2$ islands, as shown in Fig. 4.3c-f. Here, it is worthwhile to point out that the corners of 60°, 90°, 120°, and 150° in the compact structures of the $MoSe_2$ islands in Fig. 4.3c-f and highlighted in Fig. 4.10 for the case at or near the transition, originate from the inter-junctioning of two identical types of zigzag or armchair edges, one zigzag and one armchair edge, two different types of zigzag edges or two identical types of armchair edges, and one zigzag and one armchair edge, respectively. The precise shapes of the compact $MoSe_2$ islands depend on the delicate competitions between the slightly different growth rates of the armchair edge and two zigzag edges.

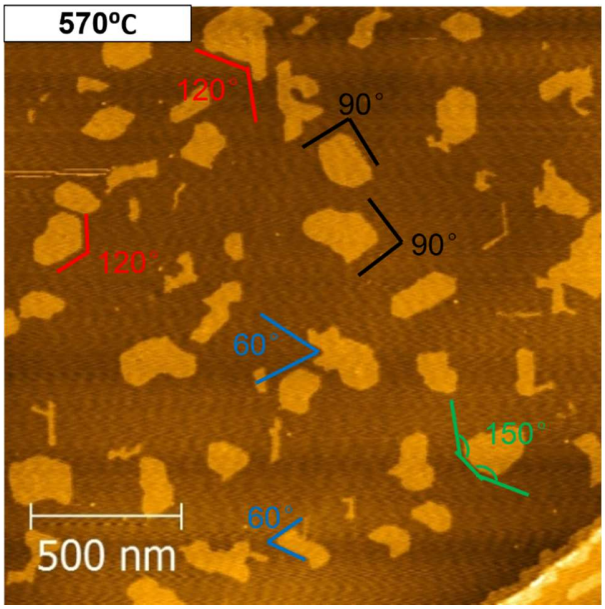

Figure 4.10: Typical angles of the corners of the 2D compact islands.

4.5 CONCLUSION AND OUTLOOKS

Controllable mass production of well-defined zigzag $MoSe_2$ nanoribbons has been achieved for the first time experimentally, and the underlying mechanism for nanoribbon growth has been revealed through synergistic efforts between controlled experiments and first-principles calculations. Such a bottom-up fabrication scheme of nanoribbons should also be transferrable to other vdW substrates, and for other TMD materials. The ready access to TMD nanoribbons as achieved in this study is expected to enable substantial future explorations of the exotic electronic, magnetic, catalytic, and transport properties of various TMD nanoribbons for potential technological applications.

Chapter 5: $MoSe_2$/hBN/Ru(0001) heterostructures

5.1 MOTIVATION

5.1.1 Brief introduction to hexagonal boron nitride

Hexagonal boron nitride (hBN) is a graphite-like layered material: each layer consists of boron and nitrogen atoms in a honeycomb lattice, with different elements occupying the inequivalent sublattices, respectively, and the neighboring layers are weakly coupled by van der Waals interaction. Bulk hBN has a direct band gap of about 5.97 eV[67]. Single-layer (SL) hBN debuted as a perfect dielectric material for graphene devices[68], but its importance is beyond that.

SL hBN on transition metal surfaces, including Ru(0001), is a very interesting platform with very rich phenomena[69–71]. It had been used as a platform to grow graphene/hBN heterostructures[72–75] and moreover, such heterostructures can be separated from the Ru(0001) substrate by using electrochemical exfoliation[76,77]. Due to the slight lattice mismatch between the hBN and Ru(0001) surfaces, a so-called "nanomesh" Moire pattern forms[69–71]. Such a Moire pattern introduces not only height corrugation on hBN[70], but also periodic modulation in the local work function[78–80]. These properties make the single layer hBN/Ru(0001) and related systems an ideal platform for investigating how the local work function impacts the electronic structure of the $MoSe_2$ overlayer grown by MBE.

5.1.2 TMD/hBN heterostructure

Graphene, hexagonal Boron Nitride (hBN), and TMD materials in conjunction form a diverse tool set for tailoring novel 2D electronic systems. One particularly powerful approach is stacking different types of vdW materials to form vdW heterostructures[81]. Many conceptual demonstrations of vdW heterostructures have been achieved by using

mechanical exfoliations of vdW layers and then stacking them together using transfer methods[68,82,83]. This exfoliation/transferring approach, however, is not scalable. An attractive and scalable approach is the direct epitaxial growth of 2D heterostructures, which has recently been shown in several systems using ambient chemical vapor depositions (CVDs)[84–91]. Nevertheless, achieving atomic scale control of contamination using ambient CVD is quite challenging. As an ultra-high-vacuum (UHV) based growth technique, molecule beam epitaxy (MBE) should provide better control of interface formation[92], although the number of 2D heterostructure systems demonstrated is more limited[17,93,94].

5.2 RESULTS

5.2.1 Growth and characterizations of $MoSe_2$/hBN/Ru(0001) heterostructures.

$MoSe_2$/hBN/Ru(0001) heterostructure is synthesized in an all UHV approach. First, single layer hBN is prepared on Ru(0001) following the standard UHV-CVD procedure[20,21]. Put briefly, hBN forms by the catalytic dehydrogenation of borazine molecules on Ru(0001) surface at proper vapor pressure and temperature. The high quality of hBN is confirmed by *in-situ* reflection high energy electron diffraction (RHEED) and STM. Shown in Fig. 5.1a is the RHEED pattern after the hBN growth on Ru(0001), with sharp spots indicating perfect crystallinity of the sample surface. Note that there are six dots arranged at hexagon corners surrounding each bright spot on the first Laue ring, reflecting the existence of a Moire pattern. Fig. 5.1b shows a typical large-scale STM image of continuous single domain hBN. A “nanomesh” moiré pattern is clearly seen. The full coverage of single-domain hBN observed here agrees with the spotty characteristic of RHEED. After a full coverage of single layer hBN, additional exposure to borazine molecule would not lead to additional growth suggesting that borazine molecules no longer have access to the catalytic

Ru(0001) surface. The zoomed-in image of the nanomesh shown in Fig. 5.1c reveals that the periodicity of the nanomesh pattern is 3.2nm, in agreement with the periodicities of 13×13 hBN and 12×12 Ru(0001) lattices[21,33]. Meanwhile, two distinct topography features on the nanomesh are seen: the lower and strongly bound regions assigned as "holes," and the higher and loosely bound regions assigned as "wires." This uneven binding causes the corrugation of the hBN, with an average amplitude of about 0.1 nm.

After confirming the high quality of hBN/Ru(0001), we transferred this sample *in-situ* to the MBE system for $MoSe_2$ growth. This all-UHV approach produces a heterostructure with a clean and sharp interface. Additional sharp and uniform RHEED streaks (indicated by red arrows) in Fig. 5.1d reflect the successful formation of flat crystalline $MoSe_2$ layers. In Fig. 5.1e, the large-scale STM image shows $MoSe_2$ islands with diameters from tens to hundreds of nanometers. In Fig. 5.1f, the top panel shows a typical $MoSe_2$ island, the inset shows an atomic resolution image taken from single layer $MoSe_2$, and the lower panel displays the height profile along the red dashed line. From the grid in the upper panel and the height profile in the lower panel, it is evident that the superstructure of the $MoSe_2$ island has the same periodicity, corrugated amplitude and phase as the underlying hBN. Surprisingly, the expected moiré pattern of $MoSe_2$ and hBN, whose periodicity is ~1nm, is not observed here. Rather the superstructure visible on the $MoSe_2$ is just a replication of the moiré pattern from the underlying hBN, evident by the match in phase and periodicity of spatial modulation.

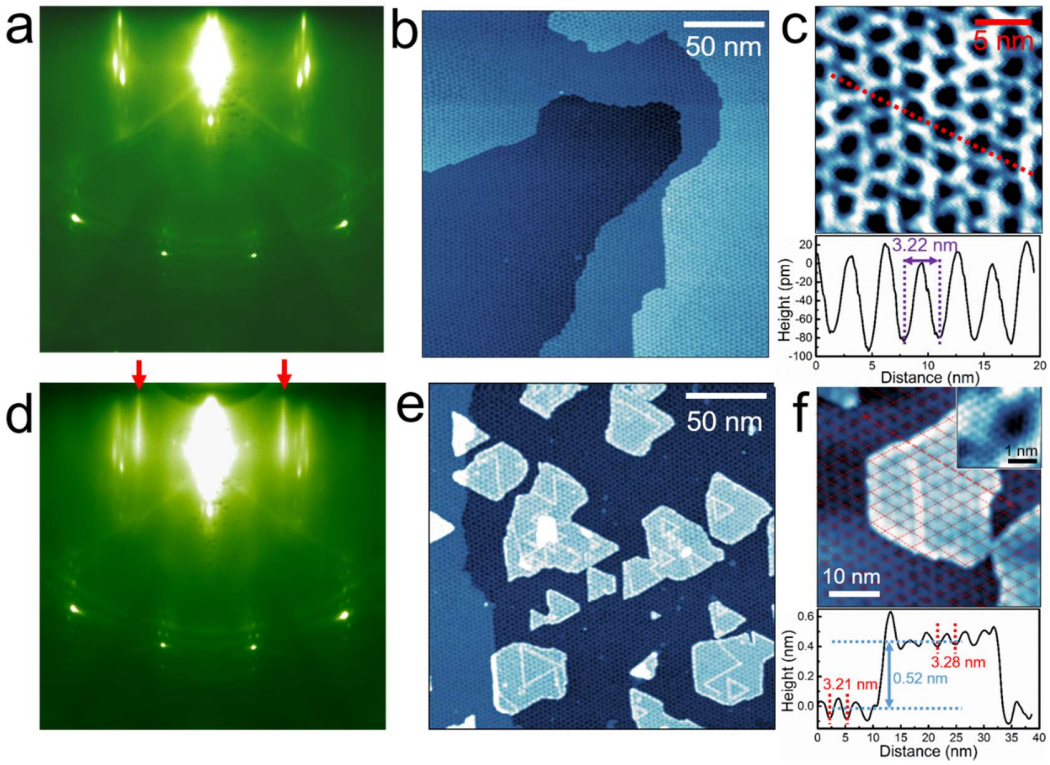

Figure 5.1 RHEED and STM characterizations of hBN/Ru(0001) and $MoSe_2$ grown on top.

a, RHEED pattern of epitaxial single layer hBN on the Ru(0001). **b**, Large-scale STM image (215 nm × 215 nm). **c**, Zoom-in STM image of hBN nanomesh. The apparent height along the red dashed line is shown in the lower panel. The periodicity and corrugation of the nanomesh are about 3.2 nm and 0.1 nm, respectively. **d**, RHEED pattern of $MoSe_2$ grown on hBN/Ru(0001). The sharp and uniform streaks (indicated by red arrows) reflect the successful synthesis of the $MoSe_2$ film. **e**, Large-scale STM image (215 nm × 215 nm) showing $MoSe_2$ islands on hBN/Ru(0001). **f**, STM image of a typical $MoSe_2$ island. The inset reveals the atomic resolution of the $MoSe_2$ layer. The corrugation of the $MoSe_2$ surface is manifested by the thin red dashed lines, which is completely in phase with that of the underlying hBN. The surface corrugation along the thick red dashed line is shown in the lower panel. All STM images were taken with Sample bias V=-2.0V and tunneling current I = 5 pA.

5.2.2 Band gap renormalization of $MoSe_2$/hBN/Ru(0001) heterostructures.

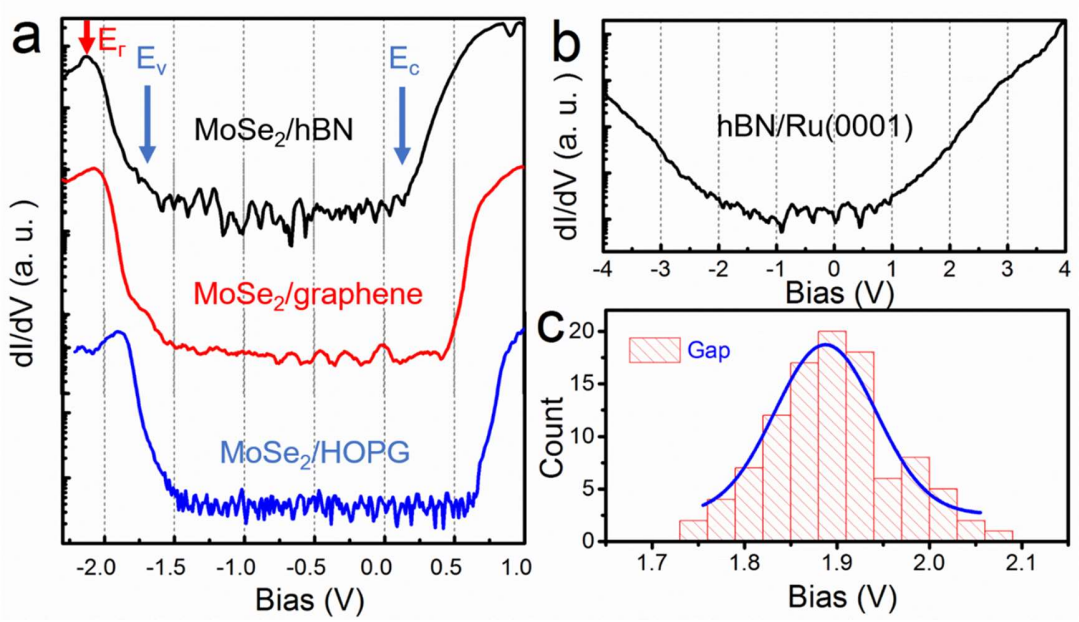

Figure 5.2 Tunneling spectroscopy of $MoSe_2$ and hBN/Ru(0001).

a, dI/dV spectra for SL-$MoSe_2$ grown on different substrates in logarithm scale. $MoSe_2$/hBN/Ru(0001), $MoSe_2$/graphene/SiC and $MoSe_2$/HOPG are shown in black, red and blue, respectively. The $MoSe_2$ layer on hBN has a smaller quasi-particle band gap (by about 0.25 eV) than that of $MoSe_2$ on graphene or graphite substrates. **b,** $log(dI)/dV$ of hBN/Ru(0001) shows the remanent metallic characteristics , due to the strong interaction between single layer hBN and Ru(0001). **c,** Statistical distribution (from 102 individual dI/dV spectrum) of the quasi-particle band gap measured for $MoSe_2$/hBN. The blue solid curve is the fitted Gaussian distribution with a mean value of1.90 eV and standard deviation 0.07 eV.

In Fig. 5.2a we show tunneling conductance spectra dI/dV of $MoSe_2$/hBN/Ru(0001), together with that of $MoSe_2$/HOPG and $MoSe_2$/graphene/SiC for comparison. In these spectra, one can identify positions of the valence band state at the Γ point (labled as E_Γ), the valence band maximum (at K point), E_V (located at ~ 0.4 eV above E_Γ), and the conduction band minimum, E_C.[1] The quasi-particle band gap is the energy difference between E_V and E_C. The spectra show that SL- $MoSe_2$ on graphene or on HOPG

[1] The methodology of the assignment of critical points in *k*-space for TMD materials is introduced in the Appendix.

have a similar quasi-particle band gap of 2.15 eV while SL-$MoSe_2$ on hBN/Ru(0001) has a smaller quasi-particle bandgap of 1.90 eV. The results show that the quasi-particle band gap of SL-$MoSe_2$ indeed depends on the supporting substrate. Nevertheless how it is renormalized does not follow the intuition that hBN should provide a better electronic isolation for $MoSe_2$ from the substrate. Also shown in Fig. 5.2b is the tunneling spectrum acquired on bare hBN region with a relatively large sample stabilization voltage of -4 V (implying a relatively large sample-to-tip distance). Interestingly significant conductance is still present in the expected "gap region" of hBN, reflecting remanent metallic characteristics. In Fig. 5.2c, we show statistical distributions of the results from 102 individual tunneling spectrum measured from different locations. The average and the standard deviation of the quasi-particle band gap of the ML $MoSe_2$/hBN/Ru(0001) is 1.90±0.07 eV.

Thus, our study convincingly demonstrate the concept of band structure renormalization in TMDs. Nevertheless, the actual manifestation of renormalization, is probably more complex than an intuitive interpretation of the substrate electrostatic screening and needs much more thorough investigations both experimentally and theoretically.

5.2.3 Work function modulation of $MoSe_2$/hBN/Ru(0001) heterostructures.

Besides the gap renormalization discussed above, we have also observed a periodic modulation of the band profile, which is associated with the work function modulation of the nanomesh moiré pattern. Location-specific STS measurements are shown in Fig. 5.3. The typical dI/dV spectra taken from $MoSe_2$ hole (red curves) and wire (blue curves) regions are plotted in both the linear scale (upper panel) and the logarithmic scale (lower panel) in Fig. 5.3a. We use the dI/dV spectra in the logarithmic scale to determine the

CBM, the VBM, and the energy of the Γ point in the valance band, Γ_V. While the band gap values and the energy differences between Γ_V and the CBM are the same for both the hole and wire regions, there is a rigid offset for the absolute values of the CBM, VBM, and Γ_V. Such an offset in the band structure is illustrated more drastically in dI/dV mappings carried out at different tip-sample bias. Fig. 5.3b-c are the topography of the same area at -2.15 V and -2.0 V, which are close to Γ_V of holes (Γ_V^H) and wires (Γ_V^W), respectively, and they look the same. However, the corresponding dI/dV mappings taken simultaneously in Fig. 4.3e-f have a completely reversed contrast; at the -2.15V wire regions, which are brighter in the topography images, have lower local density of state (LDOS), while at the -2V hole regions, darker in topography, have lower LDOS. This phenomena confirms the existence of the modulation of the $MoSe_2$ band structure. An alternative spectroscopy technique, tip-to-sample distance, Z, vs. bias sweep in the constant-current mode, is employed to determine the Γ point values. The $(\partial Z/\partial V)_I$ spectra taken from an ensemble of 120 holes and wires in Fig. 5.4 statistically determine that, Γ_V^H = -2.14±0.03 eV, Γ_V^W = -2.01±0.02 eV, and therefore the amplitude of the periodic modulation of band profile is 0.13±0.05 eV.

In addition, the $(\partial Z/\partial V)_I$ spectra in the field emission regime is employed, and the sample bias for the first field emission resonance (FER) peak is considered a good approximation of the work function of the sample[30,31]. Fig. 5.3f-g shows the local work function modulation of hBN/Ru(0001) is 0.14 eV, and for the $MoSe_2$ overlayer such modulation is 0.16 eV, both in excellent agreement with the periodic band offset observed on $MoSe_2$. From this consistency, one can conclude that the band offset in $MoSe_2$ is purely an electrostatic effect.

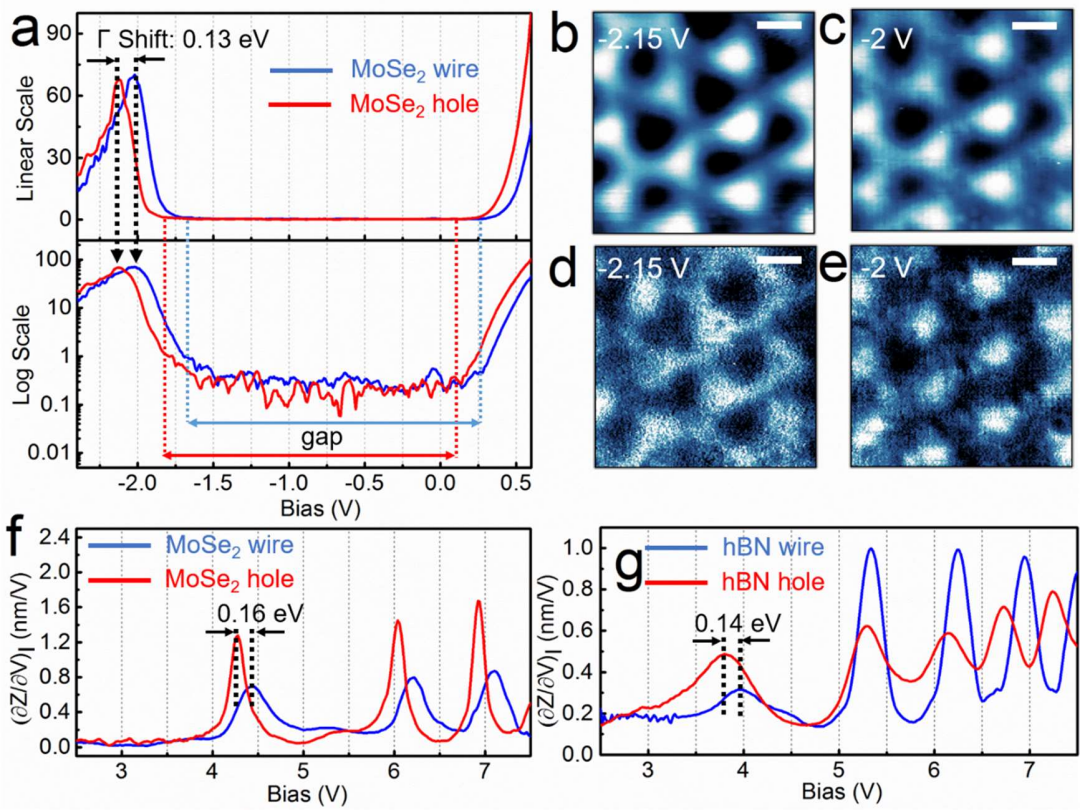

Figure 5.3 STM images and the tunneling spectra of $MoSe_2$ taken from hole and wire locations.

a, The dI/dV spectrum taken on the SL-$MoSe_2$ flake. The tunneling conductance dI/dV (with arbitrary unit) is plotted in both the linear scale (upper panel) and the logarithmic scale (lower panel). The black dashed arrows indicate the Γ points and we observed a rigid shift of the whole band structures (by about 0.13 eV) on hole and wire locations. **b,c,** Topography for the corrugated SL-$MoSe_2$. **d,e,** Corresponding dI/dV images for **b** and **c**, respectively. Scale bar: 2 nm. **f,** FER spectroscopy measured on the $MoSe_2$ wire (blue) and $MoSe_2$ hole (red). **g,** FER spectroscopy measured on the hBN wire (blue) and hBN hole (red).

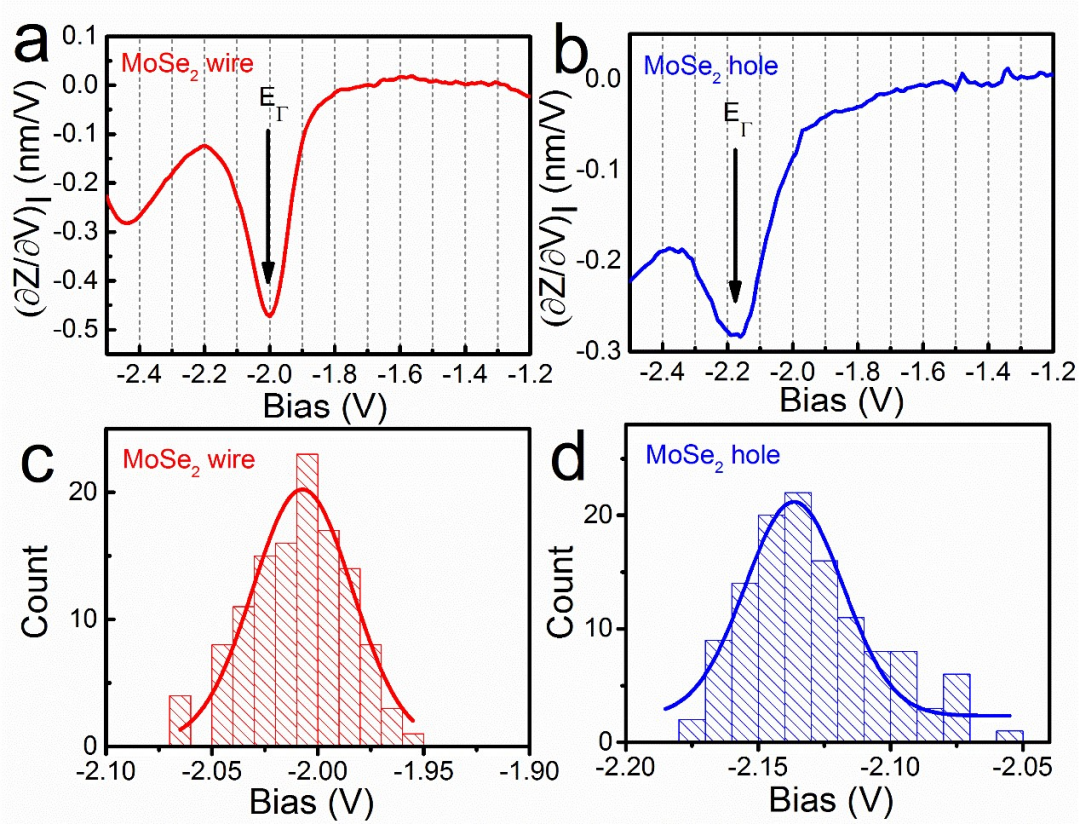

Figure 5.4 $(\partial Z/\partial V)_I$ spectra and statistical distributions of the Γ points.

a,b, Individual $(\partial Z/\partial V)_I$ spectra taken from $MoSe_2$ hole and $MoSe_2$ wire locations, respectively. The black arrows indicated the energy locations of the Γ points. **c,d,** Statistical distributions for Γ points of wire and hole, respectively (based on 120 individual $(\partial Z/\partial V)_I$ spectrum). Γ_V^H = -2.14±0.03 eV, Γ_V^W = -2.01±0.02 eV.

5.3 First Principles Calculations

The bonding and resulting change in the electronic structure of hBN on Ru(0001) can be understood by first-principles calculations, which was done by our collaborators in Georgia Institute of Technology. The observed moiré pattern in hBN/Ru(0001) corresponds to roughly 13×13 hBN on 12×12 Ru(0001), which is too large for a thorough theoretical analysis using plane waves. Instead, we used a supercell with √57×√57 h-BN

on 7×7 Ru(0001) and a small rotational angle of 6.6°, as shown in Fig. 5.5a, which provides the essential collection of different atomic registries between the layers and reliable electronic properties for them because the strain (0.08%) is very small. The relaxed atomic configuration is shown in Fig. 5.5b, indicating that a certain portion of the hBN layer is moved closer to the Ru substrate. This happens in the region near the black circle in Fig. 5.5a, in which the N atoms are approximately located right above the Ru atoms and strong bonding occurs, giving rise to a calculated interlayer distance reduction as large as 1.6 Å, in agreement with calculated results obtained previously with different supercells, basis sets, exchange-correlation functionals[34-36]. The bonding can be seen by the isosurfaces of charge transfer shown in Fig. 5.5c. In contrast, the green and purple circles mark the regions in which Ru atoms are located right below the B atoms and the center of the B-N hexagons, respectively. The interlayer interaction is weak, and these two regions are at about 3.7 Å above the Ru plane, a reasonable distance for the van der Waals interaction.

If we evaluate the electrostatic potential at 4.9 Å above the hBN layer (the average of the van der Waals layer separations of hBN and $MoSe_2$), the value in the hole region is clearly lower than that in the wire region by 0.1 eV, as shown in Fig. 5.5d. This is in excellent agreement with the relative band edge shift of SL $MoSe_2$ between the two regions as observed in the experiment. The projected density of states shown in Fig. 5.6 confirms that the significant interaction between hBN and the Ru substrate in the hole region induces states in the hBN gap, giving rise to a metallic characteristics.

Our observation of a band gap reduction of 0.25 eV for $MoSe_2$ on hBN/Ru(0001) proposes interesting possibilities of band gap renormalization in 2D materials. One probable origin is the extra screening by the states in the gap of hBN arising from the strong interaction with the substrate metal. Another possible reason is the significant corrugation (about 0.1 nm) of SL $MoSe_2$ as shown in Fig. 5.1f. In planar SL $MoSe_2$ the VBM (CBM)

is the d_{xy} and d_{x2-y2} (d_{3z2-r2}) orbitals from Mo. Any local distortion away from the perfect flatness will break the planar symmetry and induce additional hybridization between these *d* orbitals. A band gap reduction is an entirely plausible result in this situation.

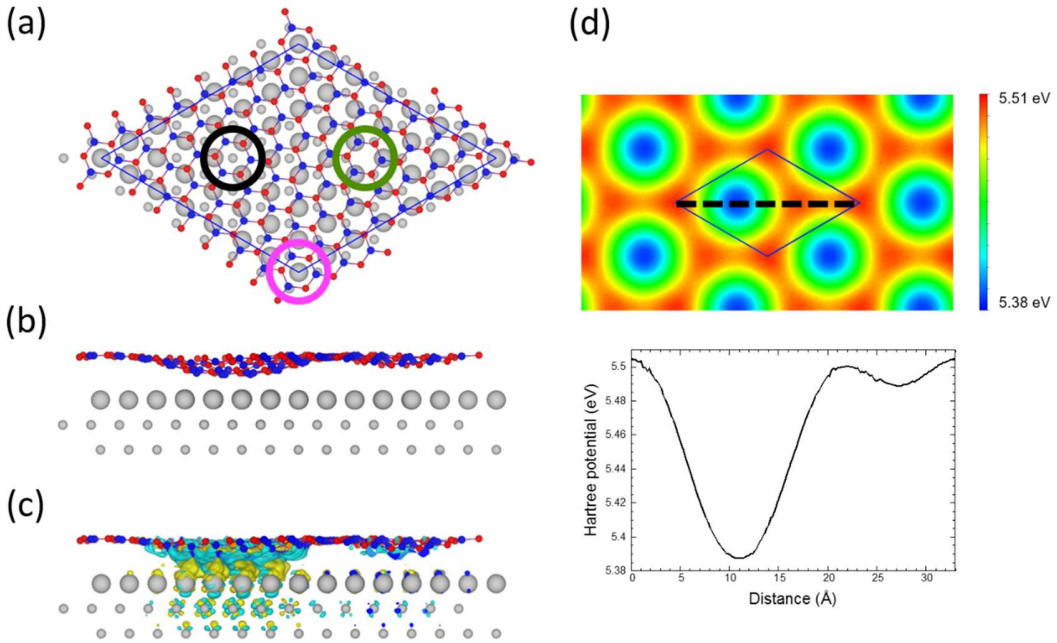

Figure 5.5 First-principles calculations for the electronic structures of hBN/Ru(0001).

a, Top view and **b,** side view of the atomic structure of √57 x √57 h-BN on 7 x 7 Ru(0001). The red, blue, and gray spheres are N, B, and Ru atoms, respectively. The black, pink, and green circles indicate the regions with N atoms at the top, fcc, and hcp sites, respectively, with respect to the Ru(0001) substrate. The distance between the h-BN and the surface Ru layers is about 3.7 Å in the regions indicated by both the green and pink circles and 2.15 Å in the region of the black circle with a maximal height difference of about 1.6 Å for the h-BN layer. **c,** Charge density difference induced by the interaction, with the yellow (blue) isosurfaces indicating an increase (decrease) in the charge density. **d,** Calculated electrostatic potential variations at the height of 4.9 Å above the h-BN layer, which corresponds to average of the interlayer distances of h-BN and $MoSe_2$. The profile along the dotted black line is also shown.

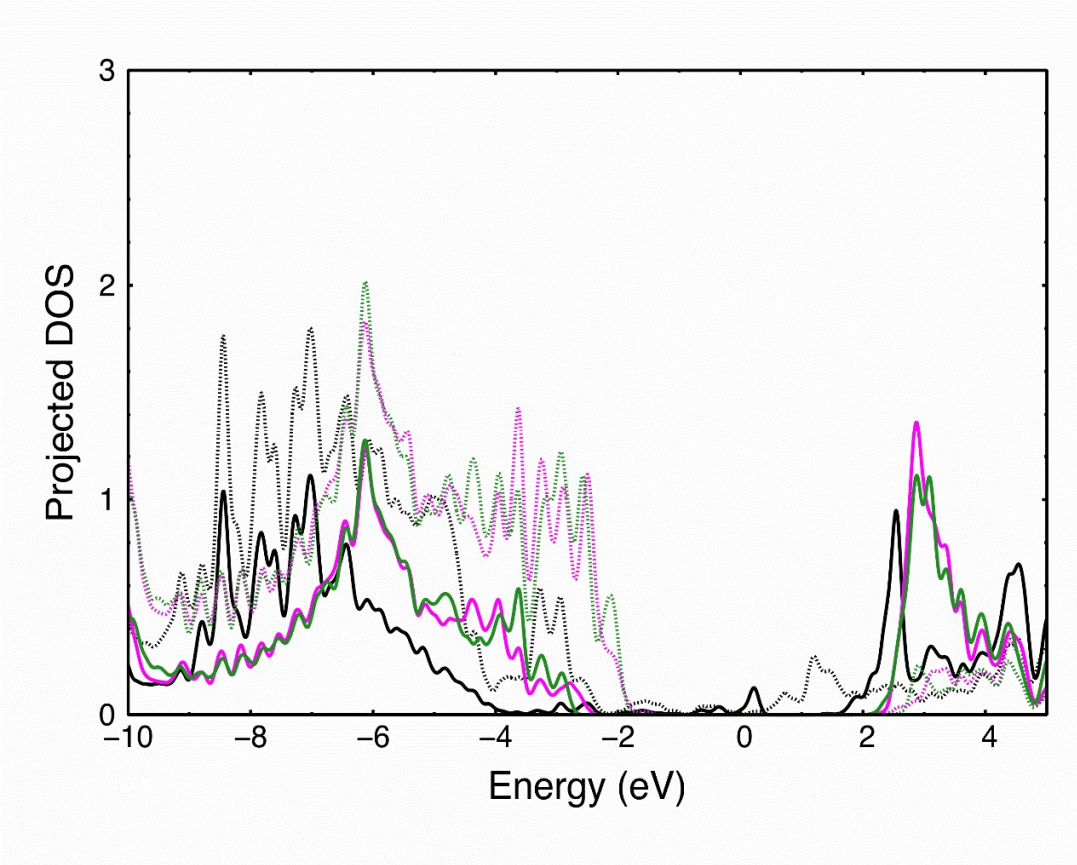

Figure 5.6 Projected density of states on the p orbitals of B (solid lines) and N (dotted lines) atoms in the regions indicated by the black, green, and purple circles in Fig. 5.5a.

In summary, we have demonstrated the successful MBE growth of single layer $MoSe_2$ islands on top of hBN/Ru(0001). Our STM/STS results have revealed that $MoSe_2$ on the strongly coupled hBN/Ru(0001) has a quasiparticle band gap of 1.90 ± 0.07 eV, 0.25 eV smaller than the results on graphite and graphene. These results, on the one hand affirm the concept of band structure renormalization due to the substrate; but on the other hand shows that the renormalization is far more complex than a simple consideration of the metallicity of the substrate and call for more thorough theoretical/experimental

investigations. In addition, we show that the local work function modulation on the hBN/Ru(0001) nanomesh structure creates a periodic template of potential modulation where the band profile of the $MoSe_2$ mimics this potential modulation precisely.

Appendices

Appendix A: TEM Method

The sample was first transferred onto a TEM grid following a previous report with minor modifications[95]. TEM images were recorded with a probe-corrected Titan ChemiSTEM (FEI, USA) which was operated at an acceleration voltage of 200 kV. The probe current was set at 47 pA with a convergent angle of 22 mrad for illumination. The inner collection angle was adjusted to be 44 mrad in order to enhance the contrast of Se atoms. The experimental TEM images shown in the main text were processed with improved Wiener-Filtering to increase the signal-to-noise ratio for better display. TEM image simulations were done using the software QSTEM with input parameters same as the experimental settings.

Appendix B: DFT Method (for Nanoribbon project)

The DFT calculations were performed using the projector-augmented wave method[96,97] implemented in the Vienna *ab initio* simulation package (VASP).[98] For the exchange-correlation functional, we used the generalized gradient approximation of Perdew, Burke, and Ernzerhof.[99] A plane-wave basis set was adopted with an energy cutoff of 350 eV. In each supercell, the vacuum layers between two neighboring ribbons are thicker than 16 Å along both the transverse and vertical directions of the ribbons. The one-dimensional Brillouin zone was sampled using a 32×1×1 Monkhorst-Pack *k*-point mesh for all the ribbons considered. All the atoms were fully relaxed by the conjugate gradient algorithm until the residual forces were less than 0.01 eV/Å.

Appendix C: DFT Method (for Heterostructure project)

We have performed first-principles calculations with density functional theory (DFT) as implemented in the Vienna Ab initio Simulation Package (VASP)[100]. We used the projector augmented wave (PAW) method[96] to treat core electrons and the Perdew-Burke-Ernzerhof (PBE) form[99] for the exchange-correlation functional with a plane-wave cutoff energy of 300 eV. The periodic slabs contain three Ru layers as the substrate and a vacuum region of about 13 Å. The bottom of the three Ru layers is fixed, while the rest two Ru layers and the hBN layer are allowed to relax during the geometry optimization.

Appendix D: STM Spectroscopy techniques

D1: Fixed-separation I-V Measurement

The tunneling current depends on both tip density of state (DOS) and the sample DOS. When the tip DOS can be simplified as s-wave, the tunneling current, or more precisely, the derivative of tunneling current with respect to the bias $\mathrm{d}I/\mathrm{d}V$, directly reflect the DOS of the sample. So the fixed-separation I-V measurement first stabilizes the tip at a certain bias and tunneling current, and then interrupts the feedback, and finally sweeps the bias and records the tunneling current and get I-V correspondence. The first order derivative of the I-V curve yields $\mathrm{d}I/\mathrm{d}V$.

An alternative route employs a lock-in amplifier, and generate $\mathrm{d}I/\mathrm{d}V$ directly. After the feedback is interrupted, a high frequency (~ 1000Hz) tiny (~ 10 mV) AC voltage ΔV is superimposed on to the bias voltage, so as a result, the tunneling current will also have an AC component, which possesses the same frequency as the ΔV and can be picked up by a lock-in amplifier. Such AC response ΔI is proportional to $\mathrm{d}I/\mathrm{d}V$.

These two routes have both been applied in my research for determining the band structure of $MoSe_2$. They gave consistent results.

D2: Fixed-current Z-V Measurement

During this spectroscopy measurement the feedback is on. When there is a change in DOS during the bias sweep, the feedback loop will change the tip-sample separation accordingly in order to keep the tunneling current. This technique is sensitive in detecting the CBM and VBM. This technique can also be employed to determine the work function of the sample, when bias sweep is in the field emission range[101,102].

Bibliography

1. Novoselov, K. S. *et al.* Electric Field Effect in Atomically Thin Carbon Films. *Science* **306,** 666–669 (2004).
2. Kikuchi, A. & Tsukada, M. Theory of STM images of CDW in transition-metal dichalcogenides. *Surf. Sci.* **326,** 195–207 (1995).
3. Straub, T. *et al.* Charge-Density-Wave Mechanism in 2H-NbSe2: Photoemission Results. *Phys. Rev. Lett.* **82,** 4504–4507 (1999).
4. Kreis, C. *et al.* Valence and conduction band states of HfS2: From bulk to a single layer. *Phys. Rev. B* **68,** 235331 (2003).
5. Mak, K. F., Lee, C., Hone, J., Shan, J. & Heinz, T. F. Atomically thin MoS2: A new direct-gap semiconductor. *Phys. Rev. Lett.* **105,** 2–5 (2010).
6. Zeng, H., Dai, J., Yao, W., Xiao, D. & Cui, X. Valley polarization in MoS2 monolayers by optical pumping. *Nat. Nanotechnol.* **7,** 490–493 (2012).
7. Li, H., Wu, J., Yin, Z. & Zhang, H. Preparation and Applications of Mechanically Exfoliated Single-Layer and Multilayer MoS 2 and WSe 2 Nanosheets. *Acc. Chem. Res.* **47,** 1067–1075 (2014).
8. Zeng, H. & Cui, X. An optical spectroscopic study on two-dimensional group-VI transition metal dichalcogenides. *Chem. Soc. Rev.* **44,** 2629–2642 (2015).
9. Liu, G., Xiao, D., Yao, Y., Xu, X. & Yao, W. Electronic structures and theoretical modelling of two-dimensional group-VIB transition metal dichalcogenides. *Chem. Soc. Rev.* **44,** 2643–2663 (2015).
10. Xu, X., Yao, W., Xiao, D. & Heinz, T. F. Spin and pseudospins in layered transition metal dichalcogenides. *Nat. Phys.* **10,** 343–350 (2014).
11. Chhowalla, M. *et al.* The chemistry of two-dimensional layered transition metal dichalcogenide nanosheets. *Nat. Chem.* **5,** 263–75 (2013).
12. Mattheiss, L. Band Structures of Transition-Metal-Dichalcogenide Layer Compounds. *Phys. Rev. B* **8,** 3719–3740 (1973).
13. Gutiérrez, H. R. *et al.* Extraordinary Room-Temperature Photoluminescence in Triangular WS 2 Monolayers. *Nano Lett.* **13,** 3447–3454 (2013).
14. Coehoorn, R. *et al.* Electronic structure of MoSe2, MoS2, and WSe2. I. Band-structure calculations and photoelectron spectroscopy. *Phys. Rev. B* **35,** 6195–6202 (1987).
15. Zhang, C., Johnson, A., Hsu, C. L., Li, L. J. & Shih, C. K. Direct imaging of band profile in single layer MoS2 on graphite: Quasiparticle energy gap, metallic edge states, and edge band bending. *Nano Lett.* **14,** 2443–2447 (2014).
16. Zhang, C. *et al.* Probing Critical Point Energies of Transition Metal Dichalcogenides: Surprising Indirect Gap of Single Layer WSe 2. *Nano Lett.* **15,** 6494–6500 (2015).
17. Ugeda, M. M. *et al.* Giant bandgap renormalization and excitonic effects in a monolayer transition metal dichalcogenide semiconductor. *Nat. Mater.* **13,** 1091–1095 (2014).
18. Tonndorf, P. *et al.* Photoluminescence emission and Raman response of monolayer

MoS2, MoSe2, and WSe2. *Opt. Express* **21,** 4908–4916 (2013).
19. Huang, J. K. *et al.* Large-area synthesis of highly crystalline WSe2 monolayers and device applications. *ACS Nano* **8,** 923–930 (2014).
20. Ajayan, P., Kim, P. & Banerjee, K. Two-dimensional van der Waals materials. *Phys. Today* **69,** 38–44 (2016).
21. Ramasubramaniam, A. Large excitonic effects in monolayers of molybdenum and tungsten dichalcogenides. *Phys. Rev. B* **86,** 115409 (2012).
22. Ding, Y. *et al.* First principles study of structural, vibrational and electronic properties of graphene-like MX2 (M=Mo, Nb, W, Ta; X=S, Se, Te) monolayers. *Phys. B Condens. Matter* **406,** 2254–2260 (2011).
23. Coehoorn, R., Haas, C. & De Groot, R. A. Electronic structure of MoSe2, MoS2, and WSe2. II. The nature of the optical band gaps. *Phys. Rev. B* **35,** 6203–6206 (1987).
24. Lebègue, S. & Eriksson, O. Electronic structure of two-dimensional crystals from ab initio theory. *Phys. Rev. B - Condens. Matter Mater. Phys.* **79,** 4–7 (2009).
25. Li, T. & Galli, G. Electronic Properties of MoS 2 Nanoparticles. *J. Phys. Chem. C* **111,** 16192–16196 (2007).
26. Zhang, Y. *et al.* Direct observation of the transition from indirect to direct bandgap in atomically thin epitaxial MoSe2. *Nat. Nanotechnol.* **9,** 111–115 (2013).
27. Herman, M. A. & Sitter, H. in 57 (Springer Berlin Heidelberg, 1996). doi:10.1007/978-3-642-80060-3
28. Ichimiya, A. & Cohen, P. I. *Reflection High-Energy Electron Diffraction*. (Cambridge University Press, 2004). doi:10.1017/CBO9780511735097
29. Zhang, Z. & Lagally, M. G. Atomistic Processes in the Early Stages of Thin-Film Growth. *Science* **276,** 377–383 (1997).
30. Qian, X., Liu, J., Fu, L. & Li, J. Quantum spin Hall effect in two-dimensional transition metal dichalcogenides. *Science* **346,** 1344–1347 (2014).
31. Zhang, C. *et al.* Visualizing band offsets and edge states in bilayer–monolayer transition metal dichalcogenides lateral heterojunction. *Nat. Commun.* **7,** 10349 (2016).
32. Novoselov, K. S. *et al.* Two-dimensional gas of massless Dirac fermions in graphene. *Nature* **438,** 197–200 (2005).
33. Zhang, Y. B., Tan, Y. W., Stormer, H. L. & Kim, P. Experimental observation of the quantum Hall effect and Berry's phase in graphene. *Nature* **438,** 201–204 (2005).
34. Lee, C., Wei, X., Kysar, J. W. & Hone, J. Measurement of the Elastic Properties and Intrinsic Strength of Monolayer Graphene. *Science* **321,** 385–388 (2008).
35. Berger, C. Electronic Confinement and Coherence in Patterned Epitaxial Graphene. *Science* **312,** 1191–1196 (2006).
36. Tan, Y. W. *et al.* Graphene at the Edge. *Science* **666,** 1705–1708 (2009).
37. Jia, X. *et al.* Controlled Formation of Sharp Zigzag and Armchair Edges in Graphitic Nanoribbons. *Science* **323,** 1701–1705 (2009).
38. Chen, J. *et al.* Optical nano-imaging of gate-tunable graphene plasmons. *Nature*

487, 77–81 (2012).
39. Son, Y. W., Cohen, M. L. & Louie, S. G. Energy gaps in graphene nanoribbons. *Phys. Rev. Lett.* **97,** 1–4 (2006).
40. Han, M. Y., Özyilmaz, B., Zhang, Y. & Kim, P. Energy Band-Gap Engineering of Graphene Nanoribbons. *Phys. Rev. Lett.* **98,** 206805 (2007).
41. Nakada, K., Fujita, M., Dresselhaus, G. & Dresselhaus, M. S. Edge state in graphene ribbons: Nanometer size effect and edge shape dependence. *Phys. Rev. B* **54,** 17954–17961 (1996).
42. Son, Y.-W., Cohen, M. L. & Louie, S. G. Half-metallic graphene nanoribbons. *Nature* **444,** 347–349 (2006).
43. Campos-Delgado, J. *et al.* Bulk Production of a New Form of sp 2 Carbon: Crystalline Graphene Nanoribbons. *Nano Lett.* **8,** 2773–2778 (2008).
44. Cai, J. *et al.* Atomically precise bottom-up fabrication of graphene nanoribbons. *Nature* **466,** 470–3 (2010).
45. Sprinkle, M. *et al.* Scalable templated growth of graphene nanoribbons on SiC. *Nat. Nanotechnol.* **5,** 727–31 (2010).
46. Cui, P. *et al.* Carbon Tetragons as Definitive Spin Switches in Narrow Zigzag Graphene Nanoribbons. *Phys. Rev. Lett.* **116,** 1–5 (2016).
47. Tapasztó, L., Dobrik, G., Lambin, P. & Biró, L. P. Tailoring the atomic structure of graphene nanoribbons by scanning tunnelling microscope lithography. *Nat. Nanotechnol.* **3,** 397–401 (2008).
48. Li, X., Wang, X., Zhang, L., Lee, S. & Dai, H. Chemically Derived, Ultrasmooth Graphene Nanoribbon Semiconductors. *Science* **319,** 1229–1232 (2008).
49. Kosynkin, D. V *et al.* Longitudinal unzipping of carbon nanotubes to form graphene nanoribbons. *Nature* **458,** 872–876 (2009).
50. Magda, G. Z. *et al.* Room-temperature magnetic order on zigzag edges of narrow graphene nanoribbons. *Nature* **514,** 608–611 (2014).
51. Kawai, S. *et al.* Superlubricity of graphene nanoribbons on gold surfaces. *Science* **351,** 957–961 (2016).
52. Kim, W. Y. & Kim, K. S. Prediction of very large values of magnetoresistance in a graphene nanoribbon device. *Nat. Nanotechnol.* **3,** 408–412 (2008).
53. Kormányos, A. *et al.* Monolayer MoS2: trigonal warping, '\Gamma-valley', and spin-orbit coupling effects. *Phys. Rev. B* **88,** 45416 (2013).
54. Kormányos, A., Zólyomi, V., Drummond, N. D. & Burkard, G. Spin-orbit coupling, quantum dots, and qubits in monolayer transition metal dichalcogenides. *Phys. Rev. X* **4,** 1–16 (2014).
55. Liu, X. *et al.* Top-down fabrication of sub-nanometre semiconducting nanoribbons derived from molybdenum disulfide sheets. *Nat. Commun.* **4,** 1776 (2013).
56. Lin, J. *et al.* Flexible metallic nanowires with self-adaptive contacts to semiconducting transition-metal dichalcogenide monolayers. *Nat. Nanotechnol.* **9,** 436–42 (2014).
57. Cai, Y., Zhang, G. & Zhang, Y. W. Polarity-reversed robust carrier mobility in monolayer MoS2 nanoribbons. *J. Am. Chem. Soc.* **136,** 6269–6275 (2014).

58. Li, Y., Zhou, Z., Zhang, S. & Chen, Z. MoS2 nanoribbons: high stability and unusual electronic and magnetic properties. *J. Am. Chem. Soc.* **130,** 16739–44 (2008).
59. Cui, P. *et al.* Distinct Reconstruction Patterns and Spin-Resolved Electronic States along the Zigzag Edges of Transition Metal Dichalcogenides. 1–6 (2015). at <http://arxiv.org/abs/1511.04287>
60. Xia, F., Wang, H., Xiao, D., Dubey, M. & Ramasubramaniam, A. Two-dimensional material nanophotonics. *Nat. Photonics* **8,** 899–907 (2014).
61. Karunadasa, H. I. *et al.* A Molecular MoS2 Edge Site Mimic for Catalytic Hydrogen Generation. *Science* **335,** 698–702 (2012).
62. Liu, H. *et al.* Dense network of one-dimensional midgap metallic modes in monolayer MoSe2 and their spatial undulations. *Phys. Rev. Lett.* **113,** 1–5 (2014).
63. Röder, H., Hahn, E., Brune, H., Bucher, J.-P. & Kern, K. Building one- and two-dimensional nanostructures by diffusion-controlled aggregation at surfaces. *Nature* **366,** 141–143 (1993).
64. Zhang, Z., Chen, X. & Lagally, M. G. Bonding-geometry dependence of fractal growth on metal surfaces. *Phys. Rev. Lett.* **73,** 1829–1832 (1994).
65. R. M. Feenstra, W. A. Thompson, and A. P. F. Real-Space Obsevation of pi-bonded chains and surface disorded on Si(111)2x1. *Phys. Rev. Lett.* **56,** 608 (1986).
66. Stroscio, J. A., Feenstra, R. M. & Fein, A. P. Electronic Structure of the Si(111)2 × 1 Surface by Scanning-Tunneling Microscopy. *Phys. Rev. Lett.* **57,** 2579–2582 (1986).
67. Watanabe, K., Taniguchi, T. & Kanda, H. Direct-bandgap properties and evidence for ultraviolet lasing of hexagonal boron nitride single crystal. *Nat. Mater.* **3,** 404–409 (2004).
68. Dean, C. R. *et al.* Boron nitride substrates for high-quality graphene electronics. *Nat. Nanotechnol.* **5,** 722–726 (2010).
69. Corso, M. Boron Nitride Nanomesh. *Science* **303,** 217–220 (2004).
70. Goriachko, A. *et al.* Self-assembly of a hexagonal boron nitride nanomesh on Ru(0001). *Langmuir* **23,** 2928–2931 (2007).
71. Laskowski, R., Blaha, P., Gallauner, T. & Schwarz, K. Single-Layer Model of the Hexagonal Boron Nitride Nanomesh on the Rh(111) Surface. *Phys. Rev. Lett.* **98,** 106802 (2007).
72. Sutter, P., Cortes, R., Lahiri, J. & Sutter, E. Interface Formation in Monolayer Graphene-Boron Nitride Heterostructures. *Nano Lett.* **12,** 4869–4874 (2012).
73. Yang, W. *et al.* Epitaxial growth of single-domain graphene on hexagonal boron nitride. *Nat. Mater.* **12,** 792–797 (2013).
74. Roth, S., Matsui, F., Greber, T. & Osterwalder, J. Chemical vapor deposition and characterization of aligned and incommensurate graphene / hexagonal boron nitride heterostack on Cu(111). *Nano Lett.* (2013). doi:10.1021/nl400815w
75. Liu, M. *et al.* Quasi-freestanding monolayer heterostructure of graphene and hexagonal boron nitride on Ir(111) with a zigzag boundary. *Nano Lett.* **14,** 6342–

6347 (2014).
76. Lu, J. *et al.* Order–disorder transition in a two-dimensional boron–carbon–nitride alloy. *Nat. Commun.* **4,** 1–7 (2013).
77. Sutter, P., Huang, Y. & Sutter, E. Nanoscale integration of two-dimensional materials by lateral heteroepitaxy. *Nano Lett.* **14,** 4846–4851 (2014).
78. Dil, H. *et al.* Surface Trapping of Atoms and Molecules with Dipole Rings. *Science* **319,** 1824–1826 (2008).
79. Joshi, S. *et al.* Boron Nitride on Cu (111): An Electronically Corrugated Monolayer. *Nano Lett.* **12,** 5821–5828 (2012).
80. Schulz, F. *et al.* Epitaxial hexagonal boron nitride on Ir(111): A work function template. *Phys. Rev. B* **89,** 235429 (2014).
81. Geim, A. K. & Grigorieva, I. V. Van der Waals heterostructures. *Nature* **499,** 419–25 (2013).
82. Haigh, S. J. *et al.* Cross-sectional imaging of individual layers and buried interfaces of graphene-based heterostructures and superlattices. *Nat. Mater.* **11,** 764–767 (2012).
83. Kretinin, A. V. *et al.* Electronic properties of graphene encapsulated with different two-dimensional atomic crystals. *Nano Lett.* **14,** 3270–3276 (2014).
84. Lin, Y. *et al.* Atomically Thin Heterostructures Based on Single-Layer Tungsten Diselenide and Graphene. *Nano Lett.* **14,** 6936–6941 (2014).
85. Rivera, P. *et al.* Observation of long-lived interlayer excitons in monolayer MoSe2-WSe2 heterostructures. *Nat. Commun.* **6,** 6242 (2015).
86. Behura, S., Nguyen, P., Che, S., Debbarma, R. & Berry, V. Large-Area, Transfer-Free, Oxide-Assisted Synthesis of Hexagonal Boron Nitride Films and Their Heterostructures with MoS 2 and WS 2. *J. Am. Chem. Soc.* **137,** 13060–13065 (2015).
87. Shi, J. *et al.* All Chemical Vapor Deposition Synthesis and Intrinsic Bandgap Observation of MoS 2 /Graphene Heterostructures. *Adv. Mater.* **27,** 7086–7092 (2015).
88. Wang, S., Wang, X. & Warner, J. H. All Chemical Vapor Deposition Growth of MoS 2 : h-BN Vertical van der Waals Heterostructures. *ACS Nano* **9,** 5246–5254 (2015).
89. Yan, A. *et al.* Direct Growth of Single- and Few-Layer MoS 2 on h-BN with Preferred Relative Rotation Angles. *Nano Lett.* **15,** 6324–6331 (2015).
90. Chiu, M.-H. *et al.* Determination of band alignment in the single-layer MoS2/WSe2 heterojunction. *Nat. Commun.* **6,** 7666 (2015).
91. Fu, L. *et al.* Direct Growth of MoS2/h-BN Heterostructures via a Sulfide-Resistant Alloy. *ACS Nano* **10,** 2063–2070 (2016).
92. Koma, A. & Yoshimura, K. Ultrasharp interfaces grown with Van der Waals epitaxy. *Surf. Sci.* **174,** 556–560 (1986).
93. Schlaf, R., Pettenkofer, C. & Jaegermann, W. Band lineup of a SnS[sub 2]/SnSe[sub 2]/SnS[sub 2] semiconductor quantum well structure prepared by van der Waals epitaxy. *J. Appl. Phys.* **85,** 6550 (1999).

94. Miwa, J. A. *et al.* Van der Waals Epitaxy of Two-Dimensional MoS2-Graphene Heterostructures in Ultrahigh Vacuum. *ACS Nano* **9,** 6502–10 (2015).
95. Koch, C. Determination of the core structure periodicity and point defect density along dislocations. *Dissertation* (2002).
96. Blöchl, P. E. Projector augmented-wave method. *Phys. Rev. B* **50,** 17953–17979 (1994).
97. Kresse, G. & Furthmu, J. Efficient iterative schemes for ab initio total-energy calculations using a plane-wave basis set ¨. *Phys. Rev. B* **54,** 11169 (1996).
98. Kresse, G. & Joubert, D. From ultrasoft pseudopotentials to the projector augmented-wave method. *Phys. Rev. B* **59,** 1758 (1999).
99. Perdew, J. P., Burke, K. & Ernzerhof, M. Generalized Gradient Approximation Made Simple. *Phys. Rev. Lett.* 3865–3868 (1996).
100. Kresse, G. & Furthmüller, J. Efficiency of ab-initio total energy calculations for metals and semiconductors using a plane-wave basis set. *Comput. Mater. Sci.* **6,** 15–50 (1996).
101. Bono, J. & Good, R. H. Conductance oscillations in scanning tunneling microscopy as a probe of the surface potential. *Surf. Sci.* **188,** 153–163 (1987).
102. Coombs, J. H. & Gimzewski, J. K. Fine structure in field emission resonances at surfaces. *J. Microsc.* **152,** 841–851 (1988).